AGU PUBLICATIONS

JGR

Journal of Geophysical Research: Planets

RESEARCH ARTICLE

10.1002/2015JE004869

High-resolution local magnetic field models for the Martian South Pole from Mars Global Surveyor data

A. Plattner[1] **and F. J. Simons**[2]

[1] Department of Earth and Environmental Sciences, California State University, Fresno, Fresno, California, USA, [2] Department of Geosciences, Princeton University, Princeton, New Jersey, USA

Key Points:

- New degree 130 model for the magnetic field of Martian South Pole from MGS data
- Slepian-type vector basis localizes inversion of low-altitude nighttime vector data
- Weakly magnetized regional model avoids leakage from nearby strong field stripes

Correspondence to:
A. Plattner,
plattner@alumni.ethz.ch

Citation:
Plattner, A., and F. J. Simons (2015), High-resolution local magnetic field models for the Martian South Pole from Mars Global Surveyor data, *J. Geophys. Res. Planets*, *120*, 1543–1566, doi:10.1002/2015JE004869.

Received 9 JUN 2015
Accepted 18 AUG 2015
Accepted article online 24 AUG 2015
Published online 26 SEP 2015

Abstract We present two high-resolution local models for the crustal magnetic field of the Martian south polar region. Models SP130 and SP130M were derived from three-component measurements made by Mars Global Surveyor at nighttime and at low altitude (<200 km). The availability area for these data covers the annulus between latitudes −76° and −87° and contains a strongly magnetized region (southern parts of Terra Sirenum) adjacent to weakly magnetized terrains (such as Prometheus Planum). Our localized field inversions take into account the region of data availability, a finite spectral bandlimit (spherical harmonic degree $L = 130$), and the varying satellite altitude at each observation point. We downward continue the local field solutions to a sphere of Martian polar radius 3376 km. While weakly magnetized areas in model SP130 contain inversion artifacts caused by strongly magnetized crust nearby, these artifacts are largely avoided in model SP130M, a mosaic of inversion results obtained by independently solving for the fields over individual subregions. Robust features of both models are magnetic stripes of alternating polarity in southern Terra Sirenum that end abruptly at the rim of Prometheus Planum, an impact crater with a weak or undetectable magnetic field. From a prominent and isolated dipole-like magnetic feature close to Australe Montes, we estimate a paleopole with a best fit location at longitude 207° and latitude 48°. From the abruptly ending magnetic field stripes, we estimate average magnetization values of up to 15 A/m.

1. Introduction

The Mars Global Surveyor (MGS) satellite mission, operated by NASA between 1996 and 2006, has yielded a wealth of knowledge about the Martian magnetic field. It confirmed the absence of an active Martian core field and led to the discovery of unexpectedly strong crustal magnetic field features. *Stevenson* [2001] provides an early review.

1.1. Modeling the Martian Field

Acuña et al. [1999] presented the first crustal magnetic field map based on observations made globally at 100 to 200 km altitude, plotting the data from the satellite mission's aerobraking phase at their corresponding altitudes. *Acuña et al.* [2001] and *Connerney et al.* [2001] improved this map by including data collected during the first few months of the satellite mission's mapping phase. *Arkani-Hamed* [2001a, 2002, 2004] and *Cain et al.* [2003] determined spherical harmonic models. Those were constructed for evaluation altitudes ranging from 120 to 370 km above the planetary surface. Most recently, *Morschhauser et al.* [2014] presented a spherical harmonic model that was downward continued onto the planet's surface (the reference sphere at radius 3394.5 km), and resolved to higher spherical harmonic degrees than previous models.

In addition to using MGS measurements to derive spherical harmonic expansions of the crustal fields, several authors have solved for crustal magnetization directly, using a variety of approaches. *Purucker et al.* [2000] calculated a crustal magnetic field model based on an equivalent-source technique for data below 200 km satellite altitude. The equivalent-source solution by *Langlais et al.* [2004] yielded magnetization vector components between ±12 A/m for an assumed 40 km thick layer. *Quesnel et al.* [2007] and *Langlais and Quesnel* [2008] presented and interpreted equivalent-source dipole models for Terra Sirenum, with local magnetizations of 32 A/m, 54 A/m, and even higher values. *Chiao et al.* [2006] applied a wavelet multiscale inversion technique to account for the difference in resolving power of the data along track versus in between the satellite tracks, generally yielding magnetization vector component values between ±15 A/m, but with considerably less power at high spherical harmonic degrees. *Whaler and Purucker* [2005] used a Green's function approach to solve for the spatially variable magnetization, yielding magnitudes up to 20 A/m for a layer of constant thickness, assumed to be 40 km thick.

Voorhies et al. [2002] and *Voorhies* [2008] used global crustal magnetic field models to estimate an average Martian magnetic layer thickness (47.8±8.4 km). Within this context, the disadvantage of using global spherical harmonic models is that their power spectrum is a whole-sphere average dominated by the signature of strong local fields compared to that of more weakly magnetized areas. For this reason, *Lewis and Simons* [2012] used scalar Slepian functions [*Wieczorek and Simons*, 2005; *Simons et al.*, 2006] to make spatially localized multitaper spectral estimates [*Wieczorek and Simons*, 2007; *Dahlen and Simons*, 2008], which they inverted for the locally applicable magnetization strengths and apparent layer thicknesses. On the basis of the correlation of these estimates with independently derived crustal-thickness estimates, *Lewis and Simons* [2012] argued for a significant involvement of the crust to explain the observed magnetic signatures.

MGS carried a second instrument to map the planet's crustal magnetic field. The electron reflectometer data analyzed by *Lillis et al.* [2004, 2008a, 2008b] and *Mitchell et al.* [2007] have proven to be a formidable resource and confirmation for the interpretation of Martian crustal magnetic fields. To cite one example, *Lillis et al.* [2010] employed a Fourier-domain Monte Carlo approach combining electron reflectometer data with magnetometer measurements to model crustal (de)magnetization around large impact basins.

1.2. Interpreting the Martian Field

The crustal magnetic field models gained from all of these investigations have had a multitude of other, diverse, uses. For instance, they have aided with the investigation of interactions between Mars and the solar wind [e.g., *Brain et al.*, 2003; *Crider*, 2004]. But in the context of our present study, their main contribution has been to play a key role in piecing together the puzzle that is the structure and evolution of the Martian lithosphere, mantle, and core. *Connerney et al.* [1999, 2005] and *Harrison* [2000] argued whether the strongly magnetized features in Terra Cimmeria and Terra Sirenum may be evidence for Martian plate tectonics. *Nimmo* [2000], *Nimmo and Tanaka* [2005], and *Ravat* [2011] interpreted these structures as dike intrusions, while *Fairén et al.* [2002] suggested they formed by converging plate boundaries.

Assuming that Mars once possessed a dipolar main field, several authors used either crustal magnetic field models or the data directly to estimate paleopole locations [e.g., *Sprenke and Baker*, 2000; *Arkani-Hamed*, 2001b; *Hood and Zakharian*, 2001; *Arkani-Hamed and Boutin*, 2004; *Frawley and Taylor*, 2004; *Boutin and Arkani-Hamed*, 2006; *Hood et al.*, 2007; *Langlais and Purucker*, 2007; *Quesnel et al.*, 2007; *Hood et al.*, 2010; *Milbury and Schubert*, 2010; *Milbury et al.*, 2012]. From their paleopole locations, *Arkani-Hamed* [2001b], *Arkani-Hamed and Boutin* [2004], *Hood et al.* [2005], *Milbury and Schubert* [2010], and *Milbury et al.* [2012] concluded that the ancient Martian dynamo underwent at least one polar reversal, and that true polar wander occurred. True polar wander is also in accordance with the deformation seen in the presumed shorelines that bound the northern plains [*Perron et al.*, 2007; *Milbury et al.*, 2012]; however, no such deformation is observed in the distribution of river deltas [*Di Achille and Hynek*, 2010].

Crustal magnetic fields are not only useful to identify traces of a true polar wander—potentially caused by the formation of the Tharsis rise—but also for unraveling the formation of Tharsis itself. *Johnson and Phillips* [2005] and *Lillis et al.* [2009] used the presence of weak crustal magnetic fields in the southern part of Tharsis and the absence of crustal magnetic fields in central and northern Tharsis to infer the evolution of the rise. *Hynek et al.* [2011] took the crustal magnetization model by *Whaler and Purucker* [2005] as a basis to track the possible plume migration that eventually might have created Tharsis.

Based on crustal magnetic field models, *Citron and Zhong* [2012] constrained the possible causes for the creation of the Martian crustal dichotomy. They argued against a giant-impactor model based on unobserved demagnetization effects that such an impact should cause in the southern hemisphere. Instead, they attributed the observed crustal magnetic field features to crustal production under a degree-one dominated mantle convection model, which is also supported by models of a single-hemisphere dynamo [*Stanley et al.*, 2008; *Amit et al.*, 2011; *Dietrich and Wicht*, 2013].

Studies of the Martian meteorite ALH84001 have shown that the Martian dynamo was active at 4 Ga [*Weiss et al.*, 2002]. *Acuña et al.* [1999], *Lillis et al.* [2008a, 2013], and *Milbury et al.* [2012] discussed the timing of the demise of the Martian dynamo based on the current crustal magnetic field. Using topographic data in combination with magnetic signatures of craters, *Acuña et al.* [1999] and *Lillis et al.* [2008a] suggested a demise at around 4.1 Ga (i.e., in the Noachian). *Milbury et al.* [2012] argued, based on magmatic demagnetization of younger volcanoes, that the Martian dynamo ceased at approximately 3.6 Ga (i.e., in the Hesperian). In order to be able to use surface structure ages to date subsurface magnetic features, there must be evidence for a unique link between the timing of the cause of magnetization or demagnetization and the timing of the surface expression. For Mars, this can be difficult in the case of volcanoes for which the magnetic and surface signatures can develop over long periods of time, as opposed to sudden demagnetization by impactors [*Lillis et al.*, 2013].

Arkani-Hamed and Boutin [2012] analyzed quasi-circular depressions in the crustal magnetic field models to determine the strength of the early Martian dynamo. They found that the dynamo was weak in the first 100 Myr of the planet's history. This stands in contrast to the Martian evolution history proposed by *Williams and Nimmo* [2004], in which a Martian core, hotter than the surrounding mantle at formation, provided the heat flux required to drive the dynamo. It is important to note that the *Williams and Nimmo* [2004] model allows for a dynamo without plate tectonics.

1.3. High Resolution, Low Noise

Two of the major challenges when calculating accurate but well-resolved crustal magnetic field models are attenuation of small-scale features due to high satellite altitude and pollution with noise from external sources such as solar wind interactions with the planet's ionosphere. The latter is particularly problematic for Mars since the planet does not possess an active core field to shield it from incoming solar wind. Most of the models discussed above achieved global coverage by a conservative selection of high-quality data obtained during the "mapping" phase of the MGS mission, which was conducted at the relatively high altitudes of 370–438 km [*Connerney et al.*, 2001].

As part of its orbit insertion, slowing down to reach a stable orbit, the satellite performed a series of highly elliptical low-altitude passes (dipping as low as 85 km) through the Martian atmosphere. During this "aerobraking" phase, the dish antenna was retracted and inactive. From the aerobraking passes, we selected those data for which the satellite was on the planet's nightside (defined by zero or negative output of the solar panels) and, from those, only the data points collected below 200 km above Mars' volumetric mean radius 3390 km. These observations cluster around the Martian south pole, in a region covering only a small fraction of the planet's surface.

To make optimal use of these local high-quality data without having to dilute them with lower quality data for complete coverage over the rest of the planet, we developed a new local magnetic field inversion method using "altitude-cognizant gradient vector Slepian functions." We note that the method used by *Lewis and Simons* [2012], briefly mentioned above, used "scalar Slepian functions" to spatiospectrally localize a global spherical harmonic power spectrum [see also *Beggan et al.*, 2013]. As do we, they achieved spatial localization via the construction of a new set of basis functions that optimizes their spatial concentration within the region of interest. In our case, however, we additionally include the satellite measurement altitude and all three vector components of an internal-source magnetic field into the optimization problem that yields the bases within which we conduct our inversions for the field itself (not its power spectral density). Our method will be fully described in section 2, whereas our data selection will receive more ample discussion in section 3.

1.4. Local Versus Global Modeling

In the complete absence of magnetic sources between the planetary surface and the satellite at altitude, the magnetic potential solves the three-dimensional Laplace equation. As a result, the magnetic field observed at different altitudes is linked by a unique mathematical relationship easily expressed in global functions, the spherical harmonics [e.g., *Backus et al.*, 1996]. The stability and conditioning of the transformation of the field values between different altitudes, and therefore the noise amplification, depend on the spherical harmonic degree. The maximum degree, the bandwidth, is a measure for the spatial resolution of the fields being represented by spherical harmonics. However, individual spherical harmonics have no "region of interest": their support is global.

Modeling local data using global functions presents new difficulties that we addressed in a particular way. Several other approaches had been proposed to reconcile the mixed global-local character of data and models (see the overview by *Schott and Thébault* [2011]). *Thébault et al.* [2006] and *Thébault* [2008] suggested replacing the governing global Laplace equation by an approximation valid within a bounded domain. Their approach led to a method called "Revised Spherical Cap Harmonic Analysis." *Holschneider et al.* [2003], *Mayer and Maier* [2006], and *Gerhards* [2012] constructed spherical wavelets from spherical harmonics. The method perhaps most closely related to our Slepian function approach is the localized spherical function approach independently introduced by *Lesur* [2006] and applied by *Lesur and Maus* [2006].

Previously, *Plattner and Simons* [2014a] discussed the use of scalar [*Simons et al.*, 2006] and vector [*Jahn and Bokor*, 2012; *Plattner et al.*, 2012; *Plattner and Simons*, 2014b] Slepian functions for magnetic field inversions. These "canonical" or "classical" Slepian functions, optimized exclusively to maximize spatial concentration within a certain region for a given bandwidth, are of great utility for inverting relatively low-bandwidth data collected at relatively low altitudes. However, at higher bandwidths and for downward continuation from higher altitudes, the noise amplification renders them unsuitable for the purposes in this paper. Here we introduce a new "altitude-cognizant" gradient vector Slepian function basis that explicitly takes the satellite height into account in the optimization problem. The construction, as will be described in section 2, overcomes the limits of the classical Slepian functions, as will furthermore be discussed more extensively in forthcoming work.

Without binning or further preprocessing the data, we fit a linear combination of altitude-cognizant vector Slepian functions to the selected data, using an iteratively reweighted (to avoid overemphasizing outliers) least squares approach. The altitude-cognizant gradient vector Slepian functions are constructed for the regions and average altitudes of the data collected. The inversion itself takes varying satellite altitude into account, but it performs best for data that are closely clustered around some average altitude. A more detailed discussion of aspects of the inversion using our approach is relegated to section 4.

In section 5, we present the resulting models. South pole crustal magnetic field model Model SP130 encompasses areas of strong magnetic fields adjacent to weak ones. Fitting and downward continuation of field solutions over both types of areas simultaneously is prone to creating ringing artifacts in the weak magnetic field area. This is hardly avoidable in global modeling, but it also presents a risk for our local approach, even when using only the highest-quality data. For this reason, we select subregions that only cover areas of roughly homogeneous field intensity and invert for crustal magnetic field models in those regions. The resulting subregional crustal magnetic field models, which we mosaic together as Model SP130M, blend in well with one another and are overall consistent with Model SP130. However, the ringing artifacts are absent from Model SP130M, and new features previously covered by those artifacts are revealed by this approach, which we discuss in some detail in section 6 before offering conclusions in section 7.

2. Problems and Solutions

For colatitude $0 \leq \theta \leq \pi$ and longitude $0 \leq \phi < 2\pi$ on the unit sphere, we define the real-valued surface spherical harmonics of degree l and order m as

$$Y_{lm}(\theta,\phi) = \begin{cases} \sqrt{2}X_{l|m|}(\theta)\cos m\phi & \text{if } -l \leq m < 0, \\ X_{l0}(\theta) & \text{if } m = 0, \\ \sqrt{2}X_{lm}(\theta)\sin m\phi & \text{if } 0 < m \leq l, \end{cases} \tag{1}$$

where we used the functions [*Dahlen and Tromp*, 1998]

$$X_{lm}(\theta) = (-1)^m \left(\frac{2l+1}{4\pi}\right)^{1/2} \left[\frac{(l-m)!}{(l+m)!}\right]^{1/2} P_{lm}(\cos\theta), \tag{2}$$

$$P_{lm}(\mu) = \frac{1}{2^l l!}\left(1-\mu^2\right)^{m/2}\left(\frac{\mathrm{d}}{\mathrm{d}\mu}\right)^{l+m}(\mu^2-1)^l. \tag{3}$$

The spherical harmonics Y_{lm} are orthonormal over the entire unit sphere.

Following *Plattner and Simons* [2014a], we construct "gradient vector" spherical harmonics

$$\boldsymbol{E}_{lm}(\theta,\phi) = \frac{(l+1)Y_{lm}\hat{\boldsymbol{r}} - \boldsymbol{\nabla}_1 Y_{lm}}{\sqrt{(l+1)(2l+1)}}, \tag{4}$$

where the spherical harmonic degrees $l = 1, \dots, L$ range up to a certain bandwidth L; for each degree l the order $m = -l, \dots, l$; and $\boldsymbol{E}_{00} = Y_{00}\hat{\boldsymbol{r}}$. The radial unit vector $\hat{\boldsymbol{r}}$ points outward from the unit sphere (in the negative vertical direction, $-Z$) and the surface gradient operator

$$\boldsymbol{\nabla}_1 = \hat{\boldsymbol{\theta}}\partial_\theta + \hat{\boldsymbol{\phi}}(\sin\theta)^{-1}\partial_\phi, \tag{5}$$

is expressed in terms of $\hat{\boldsymbol{\theta}}$, the unit vector in the colatitudinal direction (pointing south, $-N$), and $\hat{\boldsymbol{\phi}}$ in the longitudinal direction (pointing east, E).

From Maxwell's equations and the assumption that there are no magnetic sources between the planet and the satellite, there exists a scalar magnetic potential V satisfying Laplace's equation $\nabla^2 V = 0$ between the planet and the satellite. For a field arising from sources only within the planet, its gradient, $-\boldsymbol{\nabla} V = \boldsymbol{B}$, the magnetic field, is completely described by the "inner-source" vector spherical harmonics $\boldsymbol{E}_{lm}$.

The assumption of no sources between the planet's surface and the satellite is not entirely correct. Sources occur in particular within the ionosphere. These sources, however, are temporally varying, while the crustal magnetic field is stationary. Our measurements cover 2 weeks of investigation, and temporal variations are averaged out in the model calculation. In addition, we only use nighttime data to minimize noise from ionospheric fields due to solar wind interaction.

2.1. Inverse Problem Statement

A spherical harmonic representation of the magnetic potential field V at the planetary surface radius r_p, stemming only from sources within the planet, is an expansion that involves the spherical harmonic potential coefficients u_{lm},

$$V(r_p, \theta, \phi) = \sum_{l=0}^{\infty} \sum_{m=-l}^{l} u_{lm} Y_{lm}(\theta, \phi). \tag{6}$$

The corresponding magnetic vector field $\boldsymbol{B}$, evaluated at satellite radius $r_s > r_p$, is a linear combination of the inner-source gradient vector spherical harmonics $\boldsymbol{E}_{lm}$, expanded using the upward continued spherical harmonic coefficients

$$\boldsymbol{B}(r_s, \theta, \phi) = \sum_{l=0}^{\infty} \sum_{m=-l}^{l} u_{lm} A_{lm} \boldsymbol{E}_{lm}(\theta, \phi), \tag{7}$$

where we defined the upward continuation operator

$$A_{lm} = \sqrt{(l+1)(2l+1)}\, r_p^{-1} \left(\frac{r_s}{r_p}\right)^{-l-2}. \tag{8}$$

This is equivalent to the formulation by *Backus et al.* [1996]. Here we use the same notation as *Plattner and Simons* [2014a], their equation (22). Our factor A_{lm} in equation (8) contains the term r_p^{-1} because we did not scale the coefficients u_{lm} in equation (6) by the planet's radius, as is often done.

Equation (7) shows how to calculate the magnetic field at satellite radius r_s from the potential field coefficients at radius r_p. On the other hand, given a continuous data function $\boldsymbol{d}$, defined as a sum of the magnetic field $\boldsymbol{B}$ at satellite altitude r_s and a continuous noise function, and restricting our modeling to a bandlimited finite sum over the spherical harmonic degrees up to a bandwidth L, we can use equation (7) to invert for the spherical harmonic coefficients u_{lm} of the magnetic potential V due to internal sources. We choose to do this in a least squares sense, by minimizing a quadratic objective function that identifies the solution with the coefficients that are

$$\arg\min_{u_{lm}} \int_R \left(\sum_{l=0}^{L} \sum_{m=-l}^{l} u_{lm} A_{lm} \boldsymbol{E}_{lm} - \boldsymbol{d} \right)^2 \mathrm{d}\Omega, \tag{9}$$

where R is the region of the sphere Ω within which the continuous data function is available, or over which we desire to carry out the minimization. The problem statement in equation (9) is the equivalent of equation (157) of *Plattner and Simons* [2014a].

2.2. Solution by Gradient Vector Slepian Functions

A solution to equation (9) is obtained via differentiation with respect to $u_{lm}A_{lm}$, which yields

$$u_{lm} = A_{lm}^{-1} \sum_{l'=0}^{L} \sum_{m'=-l'}^{l'} K_{lm,l'm'}^{-1} \int_R \boldsymbol{E}_{l'm'} \cdot \boldsymbol{d}\, \mathrm{d}\Omega, \tag{10}$$

where the $(L+1)^2 \times (L+1)^2$ -dimensional set of elements

$$K_{lm,l'm'} = \int_R \boldsymbol{E}_{lm} \cdot \boldsymbol{E}_{l'm'} \, \mathrm{d}\Omega \tag{11}$$

defines the inner-product matrix $\mathbf{K}$ of the gradient vector spherical harmonics integrated over the observation domain, and the $K^{-1}_{lm,l'm'}$ are the elements of the inverse matrix $\mathbf{K}^{-1}$. The "localization" matrix $\mathbf{K}$ is symmetric and positive definite but extremely poorly conditioned. Hence, the inversion from regionally observed data sets at altitude is numerically unstable, very sensitive to noise in the data, and regularization is required.

As *Simons and Dahlen* [2006] discussed in the context of the corresponding scalar problem, rather than "damping" or otherwise modifying the matrix $\mathbf{K}$ prior to inversion, the operation (10) can be stabilized by expressing $\mathbf{K}^{-1}$ in terms of the orthogonal eigenvectors of $\mathbf{K}$. The approach, further discussed by *Plattner and Simons* [2014a] for the vector problem (9), amounts to finding the eigenvectors of $\mathbf{K}$ and expressing the spatial-domain solution as a truncated expansion in a downward continued version of that basis, with the unknown coefficients to be solved for.

By writing the "localization kernel" in the continuous form of equation (11), an orthogonal basis for the space of space-limited and bandlimited functions in the sense of *Slepian* [1983] can be calculated ahead of time (and for symmetric regions, very efficiently), from the geometry of the data collection area R alone, without precise reference to the actual latitudes and longitudes of the measurements at satellite altitude. The "gradient vector Slepian" eigenfunctions of equation (11) were first introduced by *Plattner and Simons* [2014a]. They are different from the "vector Slepian" functions developed by *Plattner and Simons* [2014b], which are applicable to vector fields in general, not only gradients of inner-source scalar potentials as stipulated by our definitions in equations (4) and (7).

Conceptually, the procedure of *Simons and Dahlen* [2006] and *Plattner and Simons* [2014a] amounted to first inverting for the spherical harmonic coefficients (via the intermediary of a truncated set of Slepian coefficients) that best describe the magnetic field observed at satellite altitude in the region of data availability, and subsequently, to downward continue these "localized" coefficients to the planetary surface. *Plattner and Simons* [2014a] presented a detailed but idealized analysis of the statistical performance of their method. Subsequent, unpublished, numerical experiments conducted with their methodology exactly as advocated revealed a susceptibility to noise for data collected at significant satellite altitude, when solving for high maximum spherical harmonic degrees (e.g., $L = 70$ for a region the size of Africa and for satellite altitude 6% of the planet's radius). This could be vastly improved upon, as we explain hereafter.

2.3. Solution by Altitude-Cognizant Gradient Vector Slepian Functions

The previous section discussed how *Plattner and Simons* [2014a] proposed solving equation (9) in terms of a new set of coefficients by making a truncated expansion of the unknown target function in a basis of vector-valued "gradient vector Slepian functions", constructed by diagonalization of $\mathbf{K}$ in equation (11). We refer to their method as the canonical gradient vector Slepian spatiospectral concentration eigenproblem. It is most like the classical case of Slepian and coworkers, ported to the surface of the sphere by *Simons et al.* [2006], because the initial optimization that yields the new basis only takes the geometry of the acquisition region into account and not its altitude. Any altitude effects are incorporated after the fact by upward and downward continuation of the unit sphere Slepian functions and subsequent manipulations [*Simons and Dahlen*, 2006]. The extensions to the vector case [*Plattner and Simons*, 2014a], its statistical analysis, and subsequent numerical experiments led us to now opt to solve a spatiospectral optimization problem for a new basis that is "altitude aware" from the outset.

A solution in a different form, but otherwise identical to equations (10)–(11), is obtained after differentiation equation (9) with respect to u_{lm}. We obtain

$$u_{lm} = \sum_{l'=0}^{L} \sum_{m'=-l'}^{l'} K'^{-1}{}_{lm,l'm'} \int_R A_{l'm'} \boldsymbol{E}_{l'm'} \cdot \boldsymbol{d} \, \mathrm{d}\Omega, \tag{12}$$

where $\mathbf{K}'$ is a new, square and positive-definite matrix containing the regional integrals of the upward continued gradient vector spherical harmonics, with the elemental entries

$$K'_{lm,l'm'} = A_{lm} \left(\int_R \boldsymbol{E}_{lm} \cdot \boldsymbol{E}_{l'm'} \, \mathrm{d}\Omega \right) A_{l'm'}. \tag{13}$$

The square, symmetric, and positive-definite matrix $\mathbf{K}'$ in equation (13) does not depend on any measurement values derived from the data. As did $\mathbf{K}$ in equation (11), only depends on the chosen region R, the satellite radius r_s, the planetary radius r_p, and the maximum spherical harmonic degree L.

The $(L+1)^2$ eigenvectors of $\mathbf{K}'$, ranked in decreasing eigenvalue order, $\lambda_1 \geq \lambda_2 \geq \cdots > 0$, are $\mathrm{g}_1, \mathrm{g}_2, \ldots$.

Our new approach amounts to determining a truncated (winnowed) expansion for the solution (12) in terms of the ranked eigenvectors of $\mathbf{K}'$. Let g_α be an eigenvector of $\mathbf{K}'$ with an associated αth largest eigenvalue λ_α, and let $g_{\alpha,lm}$ be its entries. We define the αth best-suited altitude-cognizant *scalar-valued* Slepian function on the planetary surface (radius r_p) via spherical harmonic expansion as

$$G_\alpha(\theta,\phi) = \sum_{l=0}^{L}\sum_{m=-l}^{l} g_{\alpha,lm} Y_{lm}(\theta,\phi), \tag{14}$$

and the αth best-suited altitude-cognizant *vector-valued* Slepian function at (an average) satellite altitude (radius r_s) as

$$\boldsymbol{G}_\alpha(\theta,\phi) = \sum_{l=0}^{L}\sum_{m=-l}^{l} g_{\alpha,lm} A_{lm} \boldsymbol{E}_{lm}(\theta,\phi). \tag{15}$$

If the data are located at *varying* satellite altitude, we can account for the actual satellite radii r by defining a correction with respect to r_s as follows:

$$\boldsymbol{G}_\alpha(r,\theta,\phi) = \sum_{l=0}^{L}\sum_{m=-l}^{l} g_{\alpha,lm} A_{lm} \left(\frac{r}{r_s}\right)^{-l-2} \boldsymbol{E}_{lm}(\theta,\phi). \tag{16}$$

The inverse problem to find the spherical harmonic expansion coefficients for the scalar magnetic potential on the planet's surface from the vector-valued data at satellite altitude is now reformulated in terms of the altitude-cognizant gradient vector Slepian functions $\boldsymbol{G}_\alpha(r,\theta,\phi)$. Instead of equation (9), the optimization is for the coefficients s_α of a truncated set in the new basis,

$$\arg\min_{s_\alpha} \int_{R'} \left(\sum_{\alpha=1}^{J} s_\alpha \boldsymbol{G}_\alpha - \boldsymbol{d}\right)^2 \mathrm{d}\Omega, \tag{17}$$

where the truncation parameter J determines the trade-off between bias and variance and should be chosen, ideally, to minimize the mean squared error of the result. For simple statistical models, the optimal J can be expressed in terms of the signal-to-noise ratio [*Simons and Dahlen*, 2006; *Plattner and Simons*, 2014a], but in practice, it may have to be iteratively determined, by trial and error.

Equation (17) contains a primed symbol, R', for the region of interest, to emphasize that the minimization can be conducted over a region that is different than the region R for which the altitude-cognizant gradient vector Slepian basis was constructed. Even though the region of interest R is built into the construction of the functions $\boldsymbol{G}$, their complete, nontruncated set, $J = (L+1)^2$, remains a basis for bandlimited inner-source magnetic vector fields *anywhere* on the sphere, so R, R', and J can be tailored with considerable freedom to the data at hand, as we discuss in section 4.

We evaluate the altitude-cognizant gradient vector Slepian functions $\boldsymbol{G}_\alpha$, $\alpha = 1, \ldots, J$, constructed for a certain region R, at the actual data locations (radius, colatitude, and longitude) available within a certain region R' using equation (16), and collect them in a matrix $\mathbf{M}$. Each row of $\mathbf{M}$ contains all three-component values of one altitude-cognizant gradient vector Slepian function evaluated at all data locations. We construct $\mathbf{d}$, the vector containing the field components (three per data location) actually observed at those locations. Solving equation (17) is then equivalent to solving a linear system of equations

$$\mathbf{M}\mathbf{M}^{\mathrm{T}}\mathbf{s} = \mathbf{M}\mathbf{d}, \tag{18}$$

where the vector $\mathbf{s}$ contains the unknown coefficients s_α from which to build our estimate of the potential field $\tilde{V}$ on the planetary radius. Irrespective of how many data points are part of the modeling, the system of equation (18) is of the dimension of $\mathbf{M}\mathbf{M}^{\mathrm{T}}$, i.e., $J \times J$. With $J \ll (L+1)^2$ typically a small number, the size reduction allows for fast iterative inversion schemes. After the construction and evaluation of the altitude-cognizant gradient vector Slepian functions via equation (16), the inversion step is the numerically most expensive part of the problem. The condition number of the linear system equation (18) depends on the chosen number J of altitude-cognizant gradient vector Slepian functions, but, with $J \ll (L+1)^2$, the system is generally well conditioned. To avoid overemphasizing data outliers, we apply a residual-reweighted least squares approach in the manner described by *Farquharson and Oldenburg* [1998]. Instead of solving equation (18), we iteratively solve

$$\mathbf{M}\mathbf{R}\mathbf{M}^{\mathsf{T}}\mathbf{s} = \mathbf{M}\mathbf{R}\mathbf{d}, \tag{19}$$

where in the first iteration the matrix $\mathbf{R}$ is the $k \times k$ identity matrix. In subsequent iterations, the diagonal matrix $\mathbf{R}$ is defined by its thresholded elements

$$R_{ii} = \max\left\{ \left|\mathbf{M}^{\mathsf{T}}\mathbf{s} - \mathbf{d}\right|_i^{-1}, \varepsilon \right\}, \tag{20}$$

where $\mathbf{s}$ is the solution coefficient vector from the previous iteration, ε is a small threshold, and $|\cdot|$ denotes the absolute value. Feeding the result for $\mathbf{s}$ back into equation (19) renders the linear problem (18) nonlinear, hence the iterations.

Finally, once we have obtained the coefficients s_α that are the entries in the vector s, we can calculate a model for the magnetic potential on the planet's surface using

$$\tilde{V}(r_p, \theta, \phi) = \sum_{\alpha=1}^{J} s_\alpha G_\alpha(\theta, \phi), \tag{21}$$

and if needed, the s_α can be converted back to u_{lm} via the altitude-cognizant gradient vector Slepian coefficients $g_{\alpha,lm}$, as in equation (14). The crustal magnetic field $\tilde{\boldsymbol{B}}(r_p, \theta, \phi)$ on the planetary surface (or elsewhere) is then easily obtained by calculating the spatial derivative $\boldsymbol{\nabla}\tilde{V}$, which is equivalent to replacing the functions G_α in equation (21) by the functions $\boldsymbol{G}_\alpha$ in equation (16). The approach discussed in this section was tested on synthetic data and applied to the MGS data set as discussed further below.

2.4. Additional Considerations

Both solution strategies proposed in sections 2.2 and 2.3 can be understood via the "continuous" formulation in equation (9). This led us to the least squares solutions of equations (10) and (12), which are formally equivalent. They differed "only" in the role played by the upward continuation operator A and its inverse, the downward continuation operator A^{-1}. However, this difference is extremely important since it asserts its influence on the form of the operators whose eigenvalues control the statistics of the resulting estimators. It is not feasible to compute numerically either equation (10) or equation (12), given the near-zero eigenvalues of $\mathbf{K}$ and $\mathbf{K}'$ which make ours an ill-posed inversion problem to begin with. Rather than devising an appropriate damping procedure [see, e.g., *Simons et al.*, 2006], we effectively made low-rank approximations and proceeded via truncated expansions of their inverses. In practice, we used the eigenvectors of the continuously defined operators (11) and (13), two different types of gradient vector Slepian functions, to formulate two new, discrete, inverse problems, which are stabilized by truncation rather than damping. The eigenvalue spectra of $\mathbf{K}^{-1}$ and $\mathbf{K}'^{-1}$ are very different, which explains the differences of the behaviors of the approaches in sections 2.2 and 2.3. The first of these approaches was discussed theoretically by *Plattner and Simons* [2014a], who also presented a suite of numerical tests. The second, in the form of equation (17), is the one that we prefer for the Martian field problem, after extensive testing on synthetic data using both approaches, which favored it for the altitude distribution of the data at hand.

Of course both procedures amount to "ranking and winnowing" of the approximate eigenvalues of the "normal matrix" $\mathbf{M}\mathbf{M}^{\mathsf{T}}$ of the inverse problem in equation (18). The truncated approximate singular-value decomposition of the "design matrix" $\mathbf{M}$ has deep roots in the analysis of geomagnetic data [e.g., *Kaula*, 1967; *Gilbert*, 1971; *Whaler and Gubbins*, 1981], as well as relatives in recent work along the same lines [e.g., *Schachtschneider et al.*, 2010, 2012]. The difference between the traditional approaches and our methods lies in the fact that we determine the new bases prior to inversion, by optimization, and based on information only derived from the idealized geometry of the acquisition domain. The continuous viewpoint by which equations (13) and (17) are constructed yields to the "discrete" inversion step of equation (18) that uses the new basis. The difference between our own two approaches, then, lies in whether the important effects of upward and downward continuation, to the average satellite altitude from the planetary surface, and back down again, are part of the initial basis optimization (as they are in section 2.3, with smaller corrections for the differential observation heights of individual data points made after the initial of optimization that yields the basis), or left for later incorporation (as in section 2.2). Especially for high satellite elevations, taking altitude effects into account for the basis, early on, leads to stably computable, efficient truncated estimators.

While the inversions in the new basis ultimately involve a smaller- and better-conditioned matrix problem, equation (18), with a J-dimensional solution vector, the construction of the altitude-cognizant gradient vector Slepian functions requires the prior eigenvalue decomposition of a potentially very large $(L+1)^2\times(L+1)^2$-dimensional matrix, equation (13). We might perhaps have kept the traditional approach and calculated the singular-value decomposition of the discretized version of equation (9) directly. Rather than altitude-cognizant gradient vector Slepian functions for a basis, we would obtain a set of empirical orthogonal functions to be truncated. At first glance, the computational costs of such an approach seem to match those of constructing altitude-cognizant gradient vector Slepian functions. The advantage of the latter is that for symmetric regions, such as spherical caps or rings, the matrix $\mathbf{K}$ whose eigenvalue decomposition we seek can be reordered into block-diagonal form with maximum block size $L+1$. Considering that the complexity of an eigenvalue decomposition of an $n\times n$ matrix is $\mathcal{O}(n^3)$ [e.g., *Allaire and Kaber*, 2008], this dramatically reduces the numerical costs of the eigenvalue decomposition of the system of equations from $\mathcal{O}(L^6)$ to $\mathcal{O}(L^3)$, with L the spherical harmonic bandwidth. This unlocks otherwise unattainably high spherical harmonic degree calculations. Besides being able to calculate them numerically efficiently, we can store the coefficients for the altitude-cognizant gradient vector Slepian functions once they are obtained for a region R, maximum spherical harmonic degree L, and satellite radius r_s, with no need to recalculate them when inverting for a new crustal magnetic field model using a different data set.

The spherical harmonic models obtained from this local method only represent the crustal field within the target area. Outside of the target area they are unconstrained. The computational efficiency for constructing altitude-cognizant gradient vector Slepian functions for spherical cap regions and the relatively small systems of equations that need to be solved to invert for crustal fields in small regions may allow, if the data permit, local resolutions of high spherical harmonic degrees. In test calculations, we have constructed, on an off-the-shelf eight-core desktop computer with 12 GB RAM, altitude-cognizant gradient vector Slepian functions for maximum spherical harmonic degree $L=500$ for a spherical cap of radial opening angle 5°. In situations where the data location altitudes vary too much, or when they cluster around two (or more) discrete altitudes, the conditioning of the matrix $\mathbf{MM}^{\mathrm{T}}$ in equation (18) might deteriorate because the radial data locations deviate too much from the altitude for which the altitude-cognizant gradient vector Slepian functions were constructed. In this case, it might be beneficial to construct dual- or multiple-altitude-cognizant gradient vector Slepian functions by changing equation (9) to minimize the (weighted) sum of two or several data misfits. All computations shown in this paper, including running hundreds of synthetic and high-dimensional examples, were performed on the commonly available multicore desktop machine mentioned above.

3. Data Selection

For our purpose of crustal magnetic field investigation, the MGS data set is of heterogeneous quality due to the varying satellite altitude and the time-variable external magnetic field strength. External field sources created by solar wind interactions with the Martian ionosphere are weaker during nighttime, in particular for the horizontal components of the field [e.g., *Brain et al.*, 2003]. Lowering the satellite altitude amplifies the recorded internal-field strength, as per the factor $(r_s/r_p)^{(-l-2)}$ in equations (7) and (8). For a higher satellite altitude, the coefficients for the higher spherical harmonic degrees l (which encode finer spatial resolution patterns) are exponentially stronger attenuated. This makes them more sensitive to noise and encumbers the recovery of these high-resolution coefficients. In its orbit insertion phase, MGS performed a series of very low-altitude passes through the atmosphere to use its drag for slowing down. Some of these aerobraking passes went as low as 80 km above mean volumetric radius of 3390 km.

To select only the highest-quality measurements, we restricted our analysis to data points collected during nighttime below 200 km above the mean volumetric radius. Such data are only available from aerobraking phase 2, in particular between 15 January to 28 January 1999. Figure 1 shows the geographic distribution of our data set, which regrettably covers only a small portion of the entire planet. Figure 1 (right) shows that the data coverage is densest between latitudes −76° and −87°. In the following, we will concentrate our investigation on this region, approximately 1.4% of the surface of Mars. When constructing the altitude-cognizant gradient vector Slepian functions, we use as the concentration domain R in equation (13) the annulus between these same latitudes. As to R', we only incorporate data south of latitude −74.5° to avoid fitting well-concentrated altitude-cognizant gradient vector Slepian functions that have weak values outside of their target region to data points outside of the region of interest, where the weak constraints would lead to increased noise sensitivity. The selected data set contains 12,861 data points, 77% of the total of 16,683

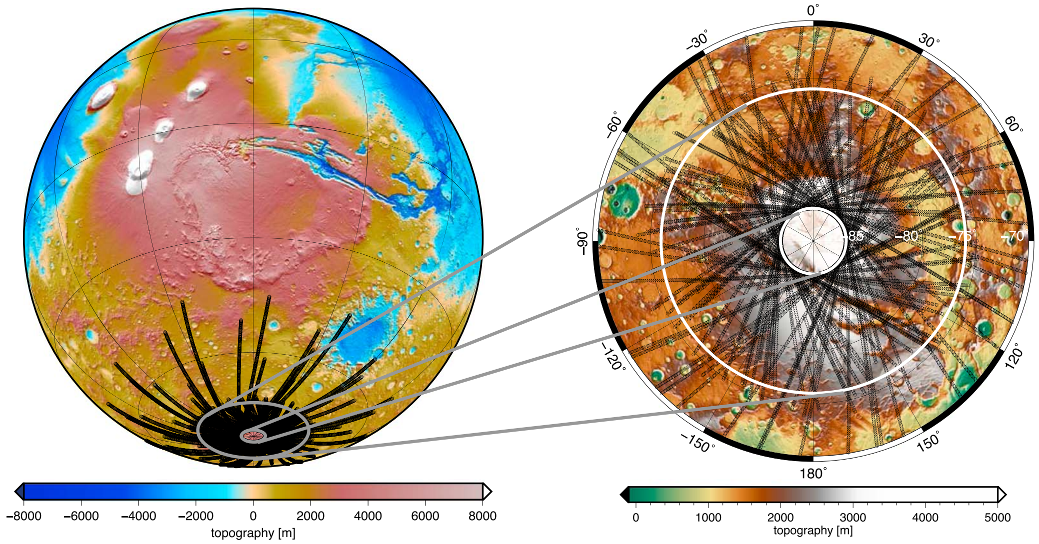

Figure 1. Topography map of Mars with location of nighttime low-altitude magnetic field data (<200 km above volumetric mean radius 3390 km). (left) Location of our area of investigation. (right) Zoom on our area of investigation delineated by the two white circles. Topography from MGS laser altimetry [*Smith et al.*, 1999].

available nighttime data below 200 km displayed in Figure 1. Average data altitude above mean volumetric radius 3390 km is 121 km.

4. Bandwidth and Model Selection

For the altitude-cognizant gradient vector Slepian approach described in section 2.3, we require selecting a region R, a maximum spherical harmonic degree L, and the number J of expansion terms in the altitude-cognizant gradient vector Slepian function sequence. Owing to the overall excellent quality of the data, the limiting factor for spatial resolution is determined not by the noise level but by the gaps between the tracks. Even though we only use data locations with latitude southward of −74.5°, where we have satellite tracks crossing, there remain some data gaps (Figure 1). These small data gaps will limit the maximum spherical harmonic degree that we can resolve. In the following, we describe the calculation of a model depending on a generic maximum spherical harmonic degree, returning to our degree selection at a later point.

For a chosen spherical harmonic degree L and the average satellite radius r_s of the data locations, we first construct and store the altitude-cognizant gradient vector Slepian functions as described by equation (15). The region R is the annulus between latitudes −76° and −87°, and the satellite altitude r_s is picked to be 135 km above the polar radius 3376 km (to 121 km above mean volumetric radius 3390 km). Since we are investigating the polar region, we set the planetary radius r_p to the polar radius, 3376 km.

We now devise a strategy to select the maximum spherical harmonic degree L and the number of active altitude-cognizant gradient vector Slepian functions J. In the first step, we will describe a way to select the number of terms J given a bandwidth L. In the second step, we compare the resulting models for a series of maximum spherical harmonic degrees L and select our model depending on the presence of features located between satellite tracks. The strategy for finding a “good” number J is described below.

We first generate 10 new data sets by adding to each datum in the original set a Gaussian random value with zero mean and standard deviation 3 nT, creating uncorrelated noise along the satellite tracks. The use of uncorrelated noise is an assumption that allows us to perform a simple test for model selection. Real along-track noise would usually be correlated. The chosen standard deviation corresponds to the estimated accuracy during aerobraking reported by *Acuña et al.* [1998] and *Brain et al.* [2003]. For each of those data sets, we invert for the crustal magnetic field for $J = 10, 20, 30, \ldots, 1000$ active altitude-cognizant gradient vector Slepian functions. By using 10 different data sets and 100 different numbers J, we run 1000 inversions per chosen spherical harmonic degree L. Conducting such an extensive survey on our desktop computer equipment is testimony to the gains in speed that can be realized by the altitude-cognizant gradient vector Slepian basis function approach used over circularly symmetric regions of spatial concentration. The magnetic potential

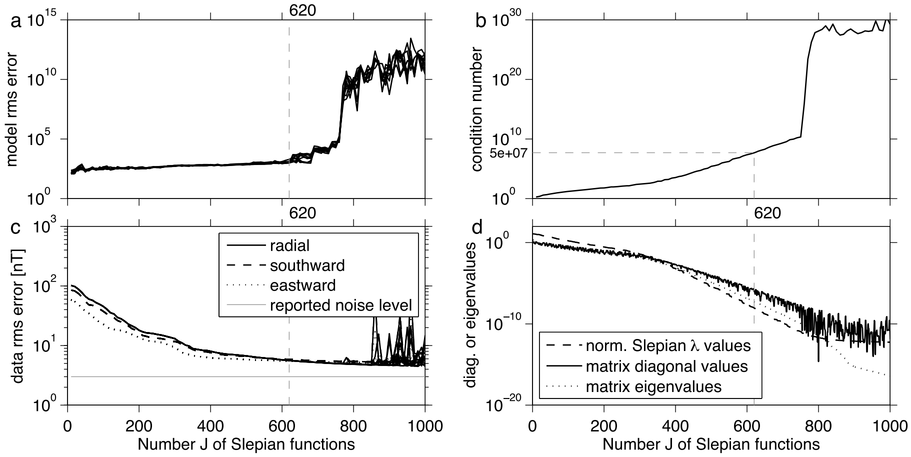

Figure 2. Perturbed solutions for the entire south polar region at the spherical harmonic bandwidth $L = 130$. (a) Model RMSE $\psi(J)$, from equation (22), for the solutions of the 10 randomly perturbed data sets. (b) Condition number of the matrix $\mathbf{M}\mathbf{M}^{\mathrm{T}}$, defined in equation (18), for different numbers J of altitude-cognizant gradient vector Slepian functions. (c) Data RMSE $\varphi_x(J)$, from equation (23), for the radial, colatitudinal, and longitudinal components of the solutions obtained from the data. (d) Diagonal values and eigenvalues of $\mathbf{M}\mathbf{M}^{\mathrm{T}}$, multiplied by the average area element for k data points in the region R, compared to the formal eigenvalues, $\lambda_1 \geq \lambda_2 \geq \cdots > 0$, of the altitude-cognizant gradient vector Slepian localization kernel $\mathbf{K}'$ defined in equation (13).

field solution derived from inverting the actual data with J active altitude-cognizant gradient vector Slepian functions, computed via equation (21), is denoted $\tilde{V}_{\mathrm{data},J}$. Each of the new solutions, derived from the randomly perturbed data, is written as $\tilde{V}_{\mathrm{pert},J}$.

To select the best crustal magnetic field model for a given spherical harmonic degree L, we calculate $\psi(J)$, the distance between the solution $\tilde{V}_{\mathrm{data},J}$ obtained from the actual data and each of the perturbed solutions $\tilde{V}_{\mathrm{pert},J}$, averaged over the target region R,

$$\psi(J) = \sqrt{\int_R \left(\tilde{V}_{\mathrm{data},J} - \tilde{V}_{\mathrm{pert},J}\right)^2 \,\mathrm{d}\Omega}. \tag{22}$$

The integration can be efficiently calculated directly from the respective spherical harmonic coefficients using the canonical scalar Slepian function localization kernels [see *Plattner and Simons*, 2014a, equation (175)], and elsewhere we refer to $\psi(J)$ as a root-mean-square model error, or "model RMSE." Figure 2a shows the 10 $\psi(J)$ curves for $L = 130$, the maximum spherical harmonic degree that we considered. We choose the optimal number of active altitude-cognizant gradient vector Slepian functions, J_{opt}, to be the largest value of J below which all the perturbed models remain visually indistinguishable (at the scale of Figure 2) in terms of the $\psi(J)$ distance. For our example, for degree $L = 130$, as seen in Figure 2a, we select $J_{\mathrm{opt}} = 620$.

We next define $\varphi_x(J)$, a root-mean-square data error or "data RMSE," between the vector components of the data $\boldsymbol{d}$ and those of the estimated field $\tilde{\boldsymbol{B}}$, as

$$\varphi_x(J) = \sqrt{\sum_{i=1}^{k} \left[\tilde{\boldsymbol{B}}_x(r_i, \theta_i, \phi_i) - (\boldsymbol{d}_x)_i\right]^2}, \tag{23}$$

where x is a placeholder for the radial ($x = \hat{\boldsymbol{r}}$), colatitudinal ($x = \hat{\boldsymbol{\theta}}$), or longitudinal ($x = \hat{\boldsymbol{\phi}}$) components, $(\boldsymbol{d}_x)_i$ is the value of the x component at the ith data location, and r_i, θ_i, and ϕ_i are the radial, colatitudinal, and longitudinal positions of the ith data location. The number of data locations is $k = 12,861$. Figure 2c shows the behavior of $\varphi_x(J)$ for our data, as a function of J.

A consistent model RMSE $\psi(J)$ between the perturbed data sets (see equation (22)), as shown when $J \leq J_{\mathrm{opt}}$ in Figure 2a, signifies that random perturbations of the order of the expected noise level do not strongly influence the result. At the same time, we must ensure that the data RMSE $\varphi_x(J)$ for all three components (see equation (23)) remains small but does not fall below the noise level. This is satisfied, as can be seen in

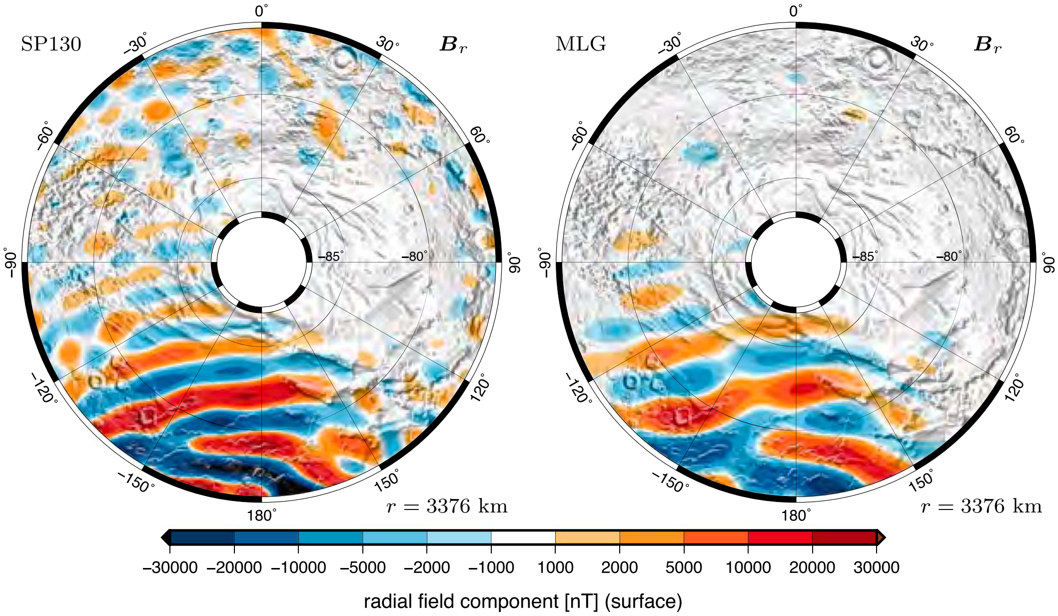

Figure 3. (left) Radial component of our crustal magnetic field model SP130 for the Martian south polar region, downward continued onto a sphere with Mars' polar radius 3376 km. (right) Global crustal magnetic field model MLG (Morschhauser Lesur Grott) by *Morschhauser et al.* [2014], downward continued to the same radius.

Figure 2c. The data RMSE exceeds the reported noise level of 3 nT and only improves marginally for $J > 620$. The sudden increase in model and data RMSE observed in both Figures 2a and 2c is brought about by the poor conditioning of the matrix $\mathbf{MM}^T$ in equation (18), illustrated by Figure 2b. From $J = 750$ upward, the condition number increases dramatically, leading to numerical instabilities in the inversion. As will be shown by us elsewhere, for a homogeneous data coverage within the region R and for data locations confined to a unique altitude r_s, the normalized diagonal and eigenvalues of the matrix $\mathbf{MM}^T$ in equation (18) converge toward the normalized eigenvalues $\lambda_1 \geq \lambda_2 \geq \cdots > 0$ of the matrix $\mathbf{K}'$ in equation (13) as the number of data points k tends to infinity. In that regime, the matrix product $\mathbf{MM}^T$ converges toward an analytic integration of the product of altitude-cognizant gradient vector Slepian functions at satellite altitude. In Figure 2d, we show that for the number of points $k = 12,861$ and at the given data locations, the diagonal and eigenvalues of $\mathbf{MM}^T$ are close to the normalized $\lambda_1 \geq \lambda_2 \geq \cdots > 0$ for $J \leq 830$.

The perturbation process allows us to select the number of altitude-cognizant gradient vector Slepian functions, $J_{\text{opt}} = 620$, to be used in the inversion at the spherical harmonic bandwidth $L = 130$. We repeated this perturbation approach for six alternative bandwidths $L = 90, 120, 130, 140, 150$, and 175, determining an optimal number of altitude-cognizant gradient vector Slepian functions for each J. Of the resulting six final models, we chose the one with the highest maximum spherical harmonic degree that did not display any significant features between the satellite tracks. For our data, the selected spherical harmonic bandwidth $L = 130$. We name the resulting model SP130. The models that we did not retain did not altogether differ much from our final model SP130 displayed in Figure 3, suggesting that our procedure is robust.

Like any other satellite data, the measurements collected by MGS do not only contain magnetic fields stemming from the planet, but they are polluted by magnetic fields from sources outside the surface described by the satellite's trajectories, from toroidal fields on the trajectory surface, and from the atmosphere. We do not remove these fields by fitting them simultaneously when solving for our model, but simply consider them as noise. As experiment to investigate the effects of external fields on our resulting models, we ran calculations in which we subtracted the external field for Mars published by *Olsen et al.* [2010] from the data at the proper altitudes before inverting. The difference between the crustal magnetic field model that resulted from using the modified satellite data, and our model made from the original data, was negligible and did not affect any of the interpreted features.

5. Result: Models SP130 and SP130M

Our preferred model SP130 encompasses an area with strongly varying magnetic field intensities that hint at the multifaceted geologic history of the Martian south pole. As described by *Head and Pratt* [2001], *Milkovich et al.* [2002], and *Milkovich and Plaut* [2008], the Martian south pole is covered by an ice cap consisting of water ice and frozen carbon dioxide. Unfortunately, except for the eastern rim of our area of investigation, most of the visible surface is of Hesperian or even Amazonian age [*Tanaka et al.*, 2014]. This makes correlations of surface features to magnetic anomalies difficult.

5.1. Model SP130

Figure 3 (left) shows the radial component of our crustal magnetic field model SP130, downward continued onto a sphere of Mars' polar radius 3376 km. We show the model within the boundaries of our region of investigation, the annulus between latitudes −87° and −76°. Figure 3 (right) shows the model MLG, made by *Morschhauser et al.* [2014], downward continued to the same 3376 km radius. The *Morschhauser et al.* [2014] model was calculated from global data including low-altitude daytime and nighttime data, and high-altitude nighttime data. Its maximum spherical harmonic degree is $L = 110$. Because their model was designed to fit data for different altitudes, it cannot resolve the crustal field with as much detail as our local approach. Nevertheless, it is remarkable that the authors managed to reveal many of the structures that we also observe in our local model.

In Figure 3 (left) around the antimeridian between longitudes −120° and +150°, we observe four "stripes" of changing polarities that run at an angle to a longitudinally oriented negative polarity stripe in the same region, north of latitude −80°. A lower resolution expression of these features is visible also in the crustal magnetic field model by *Morschhauser et al.* [2014], shown in Figure 3 (right). In both models, the stripes abruptly terminate around longitude +150°, where a region with a much weaker crustal magnetic field begins. This is the location of the Prometheus Planum impact crater. Each of the stripes is approximately 1.5 latitudinal degrees wide, corresponding to a width of 90 km. The recovered stripes narrowed slightly upon increasing the maximum spherical harmonic degree of the solutions—their physical widths could be somewhat smaller. The strong crustal field stripes are directly discernible in the satellite data at 100 km altitude, as we are to show soon.

Figure 3 shows a spatially confined magnetic anomaly in both models, around longitude 25° and latitude −81°, close to Australe Montes. Below we will use satellite data over this anomaly directly to estimate a paleopole location.

5.2. Model SP130M

In our model SP130, shown in Figure 3 (left), the intense stripes around the antimeridian, between longitudes −120° and +150°, appear to continue as weaker stripes, between longitudes −120° and −50°. Some similar stripes are also visible in the MLG model by *Morschhauser et al.* [2014], shown in Figure 3 (right). Such stripes could have a geological origin, but they could also be ringing artifacts stemming from fitting both the high-intensity stripes and an adjacent weak magnetic field with one and the same model. The appearance of these weaker stripes in both our model SP130 and in the global model MLG might suggest they are geological features. However, in this section, we will argue that they are inversion artifacts.

Since our modeling is based on a local method, we can elect to confine our investigation to a set of subregions within the south polar region instead of calculating a single regional model to fit the entire south polar data set. Thus, we construct altitude-cognizant gradient vector Slepian functions for each of these regions individually and solve for subregional models from subregional data alone.

Figure 4 shows our selected subdomains. The subregions Prometheus Planum and Australe Montes will help us further investigate the correlation between the local topographical features, an impact crater and a mountain, and the crustal magnetic field. We furthermore select a subregion in the southern part of Dorsa Argentea. This subregion contains a local magnetic feature surrounded by weaker magnetic spots, which might be artifacts. There is no visible topographical expression for this feature [*Smith et al.*, 1999]. The region labeled Western South Pole covers a large area including Cavi Angusti [*Tanaka et al.*, 2014], formed by basal melting of ice-rich deposits [*Ghatan et al.*, 2003; *Fastook et al.*, 2012], and contains the above mentioned weaker stripes that, as we are about to show, are indeed artifacts. Finally, Southern Terra Sirenum was selected to check consistency, to ascertain whether a subregional field inversion leads to the results similar to those found in our

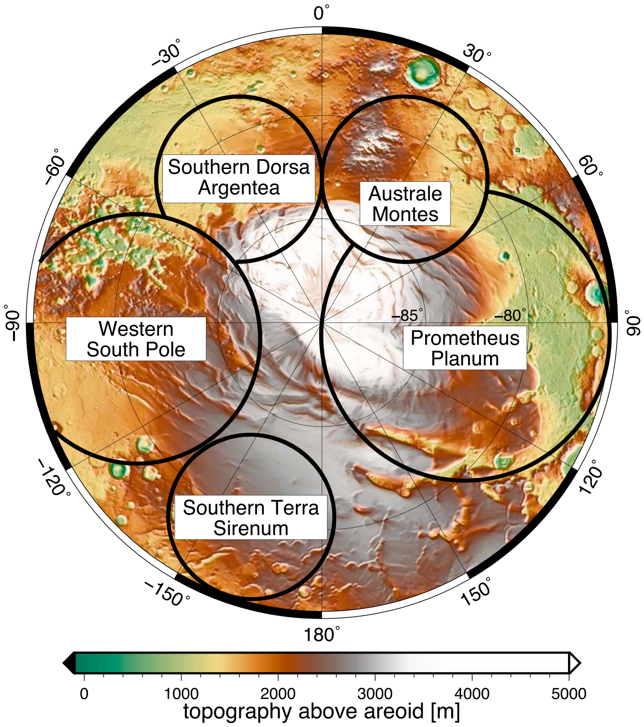

Figure 4. Subregions selected for detailed analysis, plotted over the topography of the south pole.

south polar model SP130. All of our subregions are spherical caps, whose symmetry leads to a significant reduction in the calculation time for the altitude-cognizant gradient vector Slepian functions.

For each subregion, we use select data points from the low-altitude, nighttime data set shown in Figure 1 that lie within the corresponding subregion. We retain the spherical harmonic bandwidth $L = 130$ and perform perturbation calculations as described for the entire south polar region in section 4. Table 1 summarizes the location (longitude and latitude of the center) and size (angular radius Θ) of the spherical caps constituting the subregions and lists the number J_{opt} of altitude-cognizant gradient vector Slepian functions used in the inversion for the models, as obtained from individual perturbation calculations, as well as the number of data locations within each subregion.

Figure 5 shows the resulting magnetic field models for each individual region, overlaid on the south polar crustal field model SP130 previously shown in Figure 3 simply by replacing, in the plotting, the pixel colors of SP130 within the subregions by the pixel colors of the resulting subregional models. We call this second model SP130M, where the M stands for "mosaic." Because of its sharp transitions at the subregional boundaries, SP130M itself does not possess a finite spherical harmonic expansion, but each subregional model does. The subregional solution for Southern Terra Sirenum almost perfectly matches with the south polar model SP130. For the radial and colatitudinal components, the discontinuities at the boundary of the Southern Terra Sirenum region are hardly visible in Figure 5. This gives us the reassurance that the subregional inversion does not conflict at its boundary with the whole-region inversion.

Table 1. Names, Locations, Angular Radii, Numbers of Altitude-Cognizant Gradient Vector Slepian Functions Used, and Number of Data Points for the Magnetic Field Inversion Over Selected South Polar Subregions

Name	lon	lat	Θ	J_{opt}	k
Prometheus Planum	95	−83	7	130	3931
Australe Montes	30	−82	4	60	1240
Southern Dorsa Argentea	−30	−82	4	60	1049
Western South Pole	−95	−81	6	110	2074
Southern Terra Sirenum	−160	−80	4	90	738

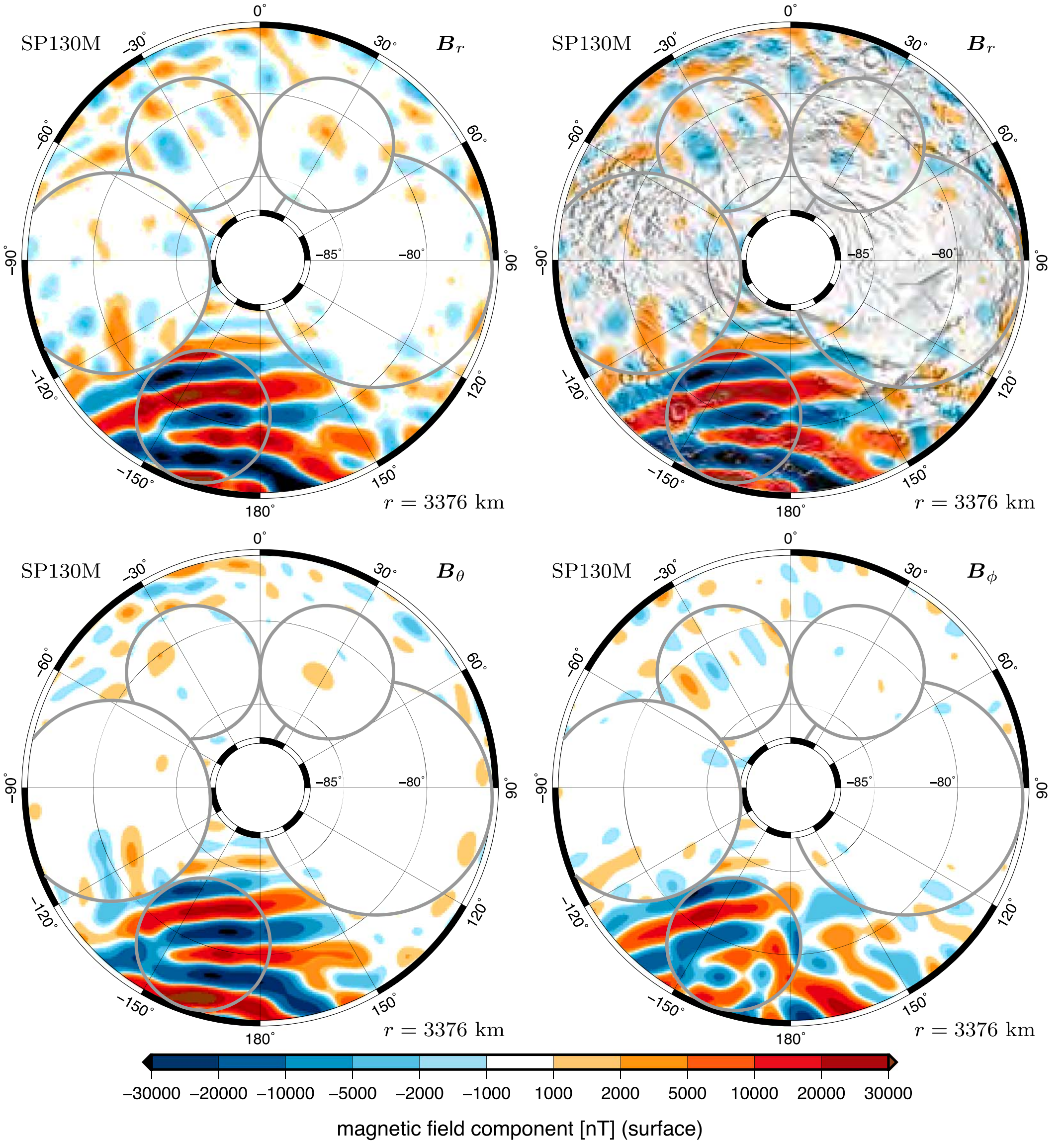

Figure 5. Our crustal magnetic field model SP130M, a mosaic overlaying the five subregional solutions over our model for the entire south pole, SP130, each downward continued to Mars polar radius 3376 km. (top left) Radial component of the field, $\boldsymbol{B}_r$. (top right) Radial component, with topographical shading. (bottom left) Colatitudinal component, $\boldsymbol{B}_\theta$. (bottom right) Longitudinal component, $\boldsymbol{B}_\phi$.

In our mosaic model SP130M, the Prometheus Planum region does not possess a significant magnetic field; this is confirmed again later by our satellite track data analysis. The electron reflectometry maps of *Lillis et al.* [2008a, 2013] confirm a weak crustal magnetic field in the Prometheus Planum region. The Australe Montes magnetic feature in our model SP130M appears as an isolated dipole. In the Southern Dorsa Argentea subregion, we observe a magnetic feature but no corresponding topographical feature. This could be explained by the younger geologic age of the surface [*Head and Pratt*, 2001; *Tanaka et al.*, 2014]. The Western South Pole subregion now reveals a previously unobserved feature that is perpendicular to the stripes in SP130. This new feature is aligned with the broader feature visible in the upward continued SP130M that we will show in the next section.

The weaker stripes that were visible in model SP130 (Figure 3) in the Western South Pole region have vanished in model SP130M (Figure 5). As an additional verification that those weaker stripes in model SP130 were indeed inversion artifacts, we will compare the models directly to the satellite data. Comparing simulated data from the models SP130, SP130M, and MLG to the measured satellite data will help us understand

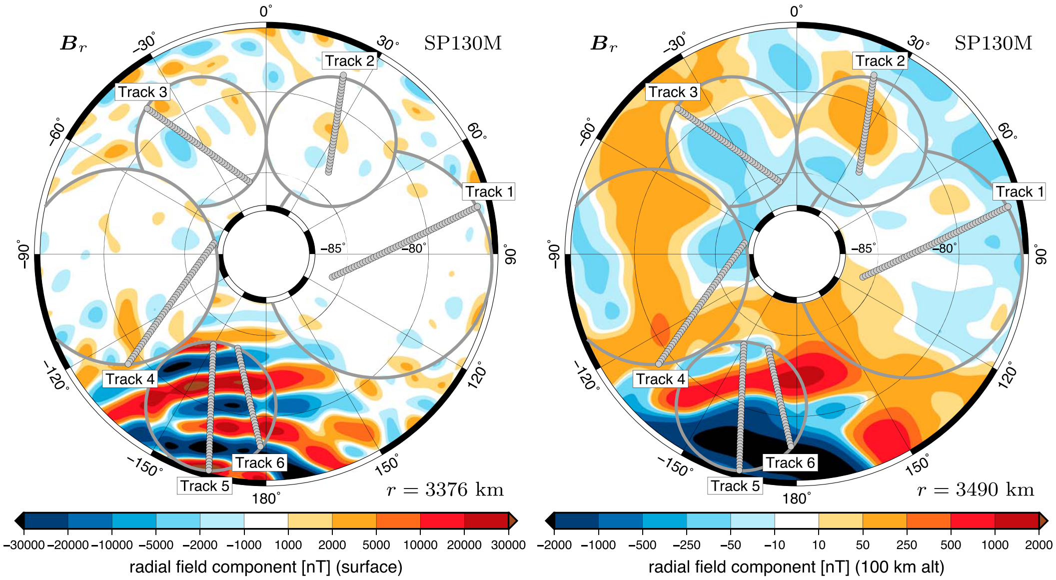

Figure 6. Locations of the tracks shown in Figure 7. (left) Tracks over the radial magnetic field on Mars' surface (sphere of radius 3376 km). (right) Tracks over the radial magnetic field at 100 km altitude above average volumetric radius 3390 km.

the difference between the models and identify the robustness of specific features. A more comprehensive distributional analysis of the model residuals is relegated to the Appendix.

5.3. Comparison With Along-Track Data

To confirm that the interpreted features stem from the data and are not artifacts from our inversion, we compare our magnetic field model to the measured data values for a selection of satellite tracks. To minimize the effects of attenuation due to altitude and noise from external fields, we only compare to nighttime satellite tracks of altitudes lower than 100 km above mean volumetric radius 3390 km. We select six tracks crossing some of the discussed features in this paper, including the Prometheus Planum crater, the Australe Montes feature, Southern Dorsa Argentea, the artificial stripes in the Western South Pole region, and the strong parallel stripes in Southern Terra Sirenum. In Figure 7, we present a comparison of the satellite data with the magnetic field model values evaluated at the satellite locations. Figure 6 shows the locations of the tracks plotted over the radial component of model SP130M on the planetary surface (left) and at 100 km above 3390 km, corresponding to satellite altitude (right).

Each row in Figure 7 corresponds to one track. The left column shows the radial component, the middle column the colatitudinal component, and the right column the longitudinal component. The horizontal axis of each panel is the latitude of the satellite location, which ranges from −87° to −76°. In each of the panels, the filled blue circles represent the measured data, with error bars given by the reported estimated precision of 3 nT [e.g., *Acuña et al.*, 1998; *Brain et al.*, 2003]. We did not preprocess or bin the data, plotting them exactly as obtained from the NASA Planetary Data System website http://pds.nasa.gov. The red curves correspond to the solutions from our individual subregional models mosaicked together in model SP130M. The green curves are evaluated from the model for the entire south polar region, SP130. The dashed black lines show the evaluated global model by *Morschhauser et al.* [2014]. For each track, we scaled the vertical axis by the field strength along the track. This explains why the error bars are clearly visible for Track 1 but collapse to a point for Tracks 5 and 6.

All three components of Track 1 show a very weak magnetic field. This track is typical for the Prometheus Planum region as can be seen in all three models SP130, SP130M, and MLG. The Australe Montes feature in Track 2 and the Southern Dorsa Argentea feature in Track 3 clearly stand out. Models SP130 and SP130M follow the data faithfully, while model MLG resembles a damped but still representative version of the features.

Track 4 lends credence to our interpretation of the stripes in Western South Pole as artifacts. Along Track 4 both models SP130 and MLG roughly follow the measured satellite data, but they also contain undulations that are not in the data. We observe that even though both models SP130 and SP130M are of the same

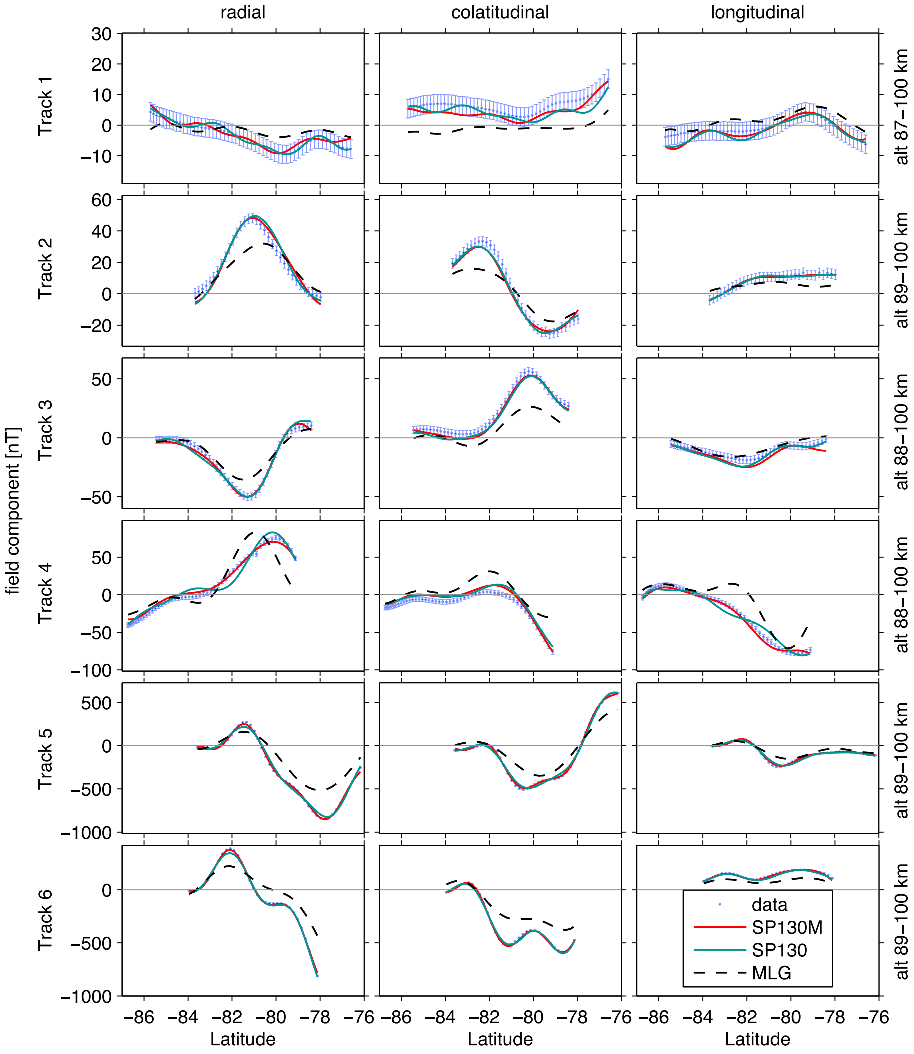

Figure 7. Along-track comparison between measured satellite data and evaluated models SP130M, SP130, and MLG. Track locations are shown in Figure 6. (left column) Radial component $\boldsymbol{B}_r$. (middle column) Colatitudinal, $\boldsymbol{B}_\theta$. (right column) Latitudinal component, $\boldsymbol{B}_\phi$. Data (filled blue circles) are shown with their ±3 nT error bars. The solid red curves represent evaluated model SP130M, solid green curves are for model SP130, and dashed black lines are for model MLG by *Morschhauser et al.* [2014].

maximum spherical harmonic degree $L = 130$, the subregional model SP130M does not show these undulations. The difference between model SP130 and model SP130M in this region is that model SP130M considered only a subset of the data used to calculate model SP130. In particular, what is missing are the strong crustal magnetic field data in the adjacent Southern Terra Sirenum region, which contain strong undulations with similar wavelength. The undulations in Track 4 are an upward continued version of the undulations visible in the Western South Pole region in Figure 3. They are characterized by relatively high amplitudes in their radial and longitudinal components but only weak amplitudes in the latitudinal component. From this evidence, we conclude that the stripes observable in SP130 and MLG in the Western South Pole subregion are artifacts created by fitting the strong fields in Southern Terra Sirenum next to what is a weakly magnetized region. Hence, SP130M reveals itself to be the more faithful version of the crustal magnetic field in that region. We do note that a higher spherical harmonic degree resolution of the entire region could allow for a sharper transition at the edge of the strongly magnetized region and hence possibly reduce the ringing effect.

Finally, Tracks 5 and 6 run through Southern Terra Sirenum. They show how the simulated data from our crustal field models closely follow the satellite data. Model SP130M shows slightly higher maximum values, which leads to the downward continued field in Figure 5 being stronger than that shown in Figure 3.

Model MLG was designed to fit both low-altitude data within the south polar region, and also mapping altitude data over the entire planet, and is limited to a maximum spherical harmonic degree $L = 110$. Considering these limitations, MLG follows Tracks 1–6 remarkably faithfully. In contrast, our altitude-cognizant gradient vector Slepian function solutions were designed to only fit the data points within the region and with a higher maximum spherical harmonic degree $L = 130$. This was possible owing to the localization of our approach and its computational efficiency.

6. Examples of Model Interpretation

Two important features are visible in both of our new models SP130 and SP130M, and in model MLG by *Morschhauser et al.* [2014]. The first is an isolated dipolar feature close to Australe Montes. The second are the stripes of strong magnetic fields with alternating polarity, which end abruptly at the boundary of Prometheus Planum. In the following, we give examples of their interpretation. We do this solely to provide guidance for future work. As to the dipolar feature, one might well argue that it is not "special" enough to merit sustained attention. As to determining the causative origin of the stripes, we should bear in mind that the amplitude of their anomaly is not particularly well constrained. While we have managed to provide an objective justification for the number of terms in the altitude-cognizant gradient vector Slepian expansion J_{opt}, we must remain aware that the strength of the recovered anomalies varies with the choice of L and J_{opt}, which complicates their quantitative geological interpretation.

6.1. A Paleopole for Australe Montes

We first investigate the feature located at longitude 25°, latitude −81°, close to Australe Montes. This crustal magnetic field feature resembles the signature of a shallowly buried magnetic dipole. It can be seen in our model SP130 (Figure 3), model SP130M (Figure 5), in the satellite Track 2 data (Figure 7), and in the spatial satellite data renditions of Figure 8. The associated magnetic field reaches 50 nT, which is roughly 10 times the expected noise level. Similar to *Hood and Zakharian* [2001] and *Langlais and Purucker* [2007], we fit a single magnetic dipole to the data and estimate the location of the corresponding paleopole of a Martian-centered dipolar core field. We fit the dipole using an iterative least squares approach using Matlab's `fsolve.m` function in combination with iteratively reweighting the residuals to reduce dependence on data outliers. The depth of the dipole was set to 5 km below the surface.

To assess the uncertainty of our paleopole inversion, we ran bootstrapped versions of the dipole fitting for a series of data subsets. Figure 8 shows an example of a fitted dipole compared to the actual data values. As our data subsets, we selected satellite measurements that were taken below 150 km above mean Martian radius at nighttime, from within spherical caps of varying angular radii and center locations. For the cap radii, we chose 4°, 5°, and 6°. For the center points, we chose longitudes 20°, 20.5°,…,30°, and latitudes −80°, −80.1°,…,−81°.

Figure 9 shows the paleopoles resulting from our bootstrapping procedure. Our estimated north poles cluster in an area between longitudes 170° and 230°, and between latitudes 20° and 70°. Each of the north poles is represented by a filled gray circle. The median of the bootstrapped paleopoles, marked by a green star, is located at longitude 207°, latitude 48°. This paleo-north pole location is consistent with the highest concentration of paleopole location reports summarized by *Hood et al.* [2005] and *Milbury and Schubert* [2010].

The presence of a mountain with Hesperian surface age [*Tanaka et al.*, 2014] associated with an older crustal magnetic field signature does not contradict that the mountain originally formed when the magnetic field was active, in the Noachian. Later eruptions might have reset the surface age. A magmatic episode associated with later eruptions could have led to a demagnetization of the crust close to the topographical expression, after the Martian dynamo had shut down. This could explain why the dipolar feature is slightly offset from Australe Montes. It might be part of an ancient magma chamber that did not get remagnetized when the magma path changed. Once again, we caution for the overinterpretation of our results, which should be developed with full consideration of the Martian geological structure and evolution.

6.2. Magnetization From Stripes

Strong magnetic field stripes are visible around longitude 180° in our models SP130 (Figure 3) and SP130M (Figure 5). They are abruptly truncated at the rim of the Prometheus Planum crater. We estimate an average crustal magnetization for these features assuming that they are caused by horizontal rectangular prisms with widths equal to the observed feature width of $\omega = 100$ km and depths equal to the demagnetization depth of the impact crater. Following *Nimmo and Gilmore* [2001], we assume a minimum impact demagnetization

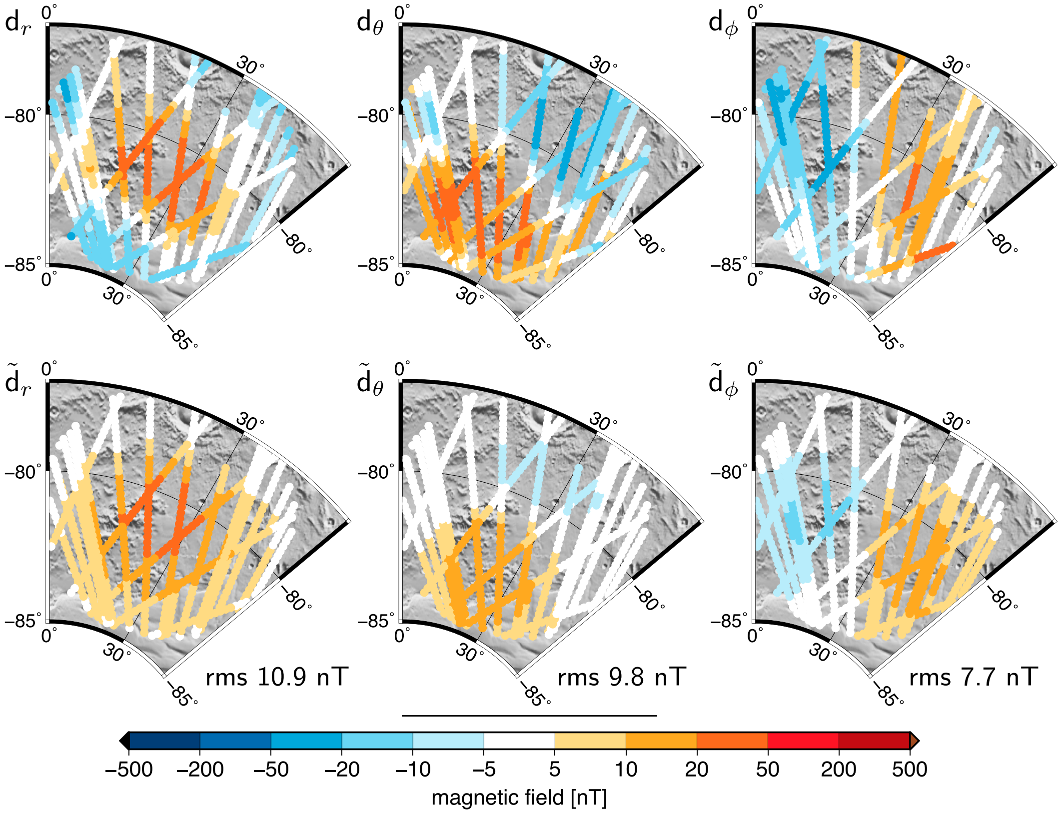

Figure 8. Comparison between three-component satellite measurements (d_r, d_θ, and d_ϕ) and a fitted dipole model ($\tilde{d}_r$, $\tilde{d}_\theta$, and $\tilde{d}_\phi$) for measurements below 150 km above mean radius 3390 km located within a spherical cap of angular radius 6° centered at longitude 24.5° and latitude −80.5°. The fitted dipole is located at longitude 23.4°, latitude −80.3°, has inclination −72.5° and declination 178.2°, and a strength of 1.23×10^5 Am^2. The corresponding paleopole for this dipole is located at longitude 202° and latitude 48°. The root-mean-square misfit is reported in the bottom right for each component.

depth of 0.04 crater diameters. For Prometheus Planum, this leads to a demagnetization (bottom) depth of $\zeta = 33$ km, close to or shallower than the Curie depth of magnetite and hematite for Mars at 4 Ga [*Nimmo and Gilmore*, 2001; *Nimmo and Stevenson*, 2001; *Dunlop and Arkani-Hamed*, 2005]. We assume that the prism is homogeneously magnetized with unknown magnetization strength M and direction radially away from the planet.

Following *Blakely* [1995] (equation (5.17)), we calculate the vertical component of the magnetic field created by this prism, observed on the surface, directly above its axis, via the relation

$$\boldsymbol{B}_z = 2\frac{\mu_0}{4\pi}\int_{-\omega/2}^{\omega/2}\int_{\zeta}^{\delta}\frac{M}{x^2+z^2}\left(\frac{2z^2}{x^2+z^2}+1\right)\,\mathrm{d}x\,\mathrm{d}z. \tag{24}$$

Here x and z are the Cartesian coordinates of the cross section of the prism; z is the vertical axis, x is the horizontal axis perpendicular to the strike of the prism, δ, ζ, and ω are the top, bottom, and width of the prism, respectively, and μ_0 is the magnetic permeability of free space. Taking the maximum radial component crustal magnetic field strength on the planetary surface from our model SP130M, we solve for the magnetization strength and depth, which, as we caution, are only poorly constrained.

In our model SP130M, the maximum radial component of the crustal magnetic field on the planet's surface ($r = 3376$ km) over the stripe features around longitude 180° is 63,000 nT, in line with some previous estimates [e.g., *Langlais and Quesnel*, 2008]. Using equation (24) and assuming that the prisms extend from 1 km below the surface down to 33 km depth, we calculate a maximum average magnetization of $M = 15$ A/m. This value is below Martian crustal field magnetization estimates by, for example, *Nimmo and Gilmore* [2001], *Hood et al.* [2010], and *Ravat* [2011]. It is within the range of terrestrial basaltic rocks which can be magnetized up to 20–30 A/m [*Nimmo and Tanaka*, 2005, and references therein].

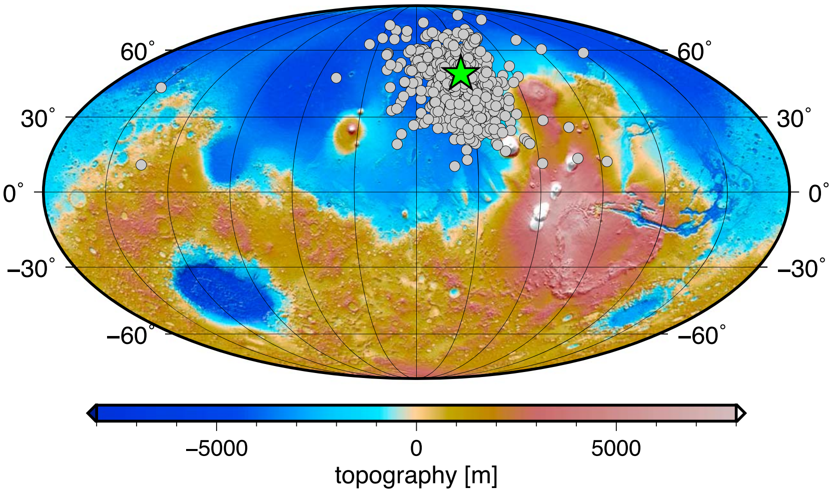

Figure 9. Bootstrapping results for the paleopole location of the Australe Montes magnetic feature. Projection is Mollweide centered at longitude 180°. Filled gray circles show paleopole positions obtained from a range of data subsets. The green star represents the median of the paleo-north locations for the Australe Montes data at longitude 207°, latitude 48°.

7. Conclusions

We have presented two new crustal magnetic field models of the Martian South Pole, SP130 and SP130M, obtained from the inversion of low-altitude vector magnetometry data collected during nighttime by the MGS satellite. Our inversion was conducted using a basis given by an optimal linear combination of vector spherical harmonics, termed altitude-cognizant gradient vector Slepian functions. These were constructed to localize information from data collected at altitude over regional and subregional domains of interest. The subregional modeling steers clear of artifacts that arise when strong crustal magnetic field features are modeled adjacent to weak fields. Our models highlight the strong heterogeneity of the Martian crustal magnetic field around its geographic South Pole and give clues to its multifaceted geological history.

Our paper focused on the inverse problem that is the modeling of the Martian crustal magnetic field from noisy, three-component data collected at varying satellite altitude. However, several previously only vaguely visible, or even unknown, features are robustly present in our models, and we provided tentative interpretations for their origin. We calculated a paleopole location from an isolated dipolar magnetic feature close to Australe Montes. From the strong magnetic field stripes in Southern Terra Sirenum, which are close to Prometheus Planum, a very weakly or nonmagnetized impact crater, we estimated maximum magnetization depth and hence, an average crustal magnetization.

Appendix A: Distributions of Data and Residuals

Figure A1 shows the distributions of data prior to fitting, and of the residuals after fitting, for the entire south polar region (model SP130) and (from model SP130M) for the weakly magnetized Prometheus Planum and the strongly magnetized Southern Terra Sirenum. While many of the data distributions are not Gaussian, their residuals follow a normal distribution. The means, μ, of the residuals for all three regions and for each vector component, are close to zero, and their standard deviations, σ, are substantially reduced compared to the standard deviations of the data. Figures A1a–A1c show the radial, colatitudinal, and longitudinal data histograms with a best fitting normal distribution for the entire south polar region. Most of the data lie within 1 standard deviation from the mean of −9.27 nT, but 2% of the data are more than 4 standard deviations away from the mean. These strong data values are located in the Southern Terra Sirenum region. The residuals of our model SP130, Figures A1d–A1f, are mostly normally distributed with means close to zero and standard deviation closest to the reported estimated noise level of 3 nT. Figures A1g and A1h show the data distribution for the Southern Terra Sirenum region. These are strongly non-Gaussian, with standard deviations of 116–284 nT. Our residuals for this region, Figures A1j–A1l, have a standard deviation of 7–8 nT, while, at the same time, most residuals are closer to the mean than the best fitting normal distribution would predict. For Prometheus Planum, Figures A1m–A1o show the magnetic field data to be generally weak and, in the case of

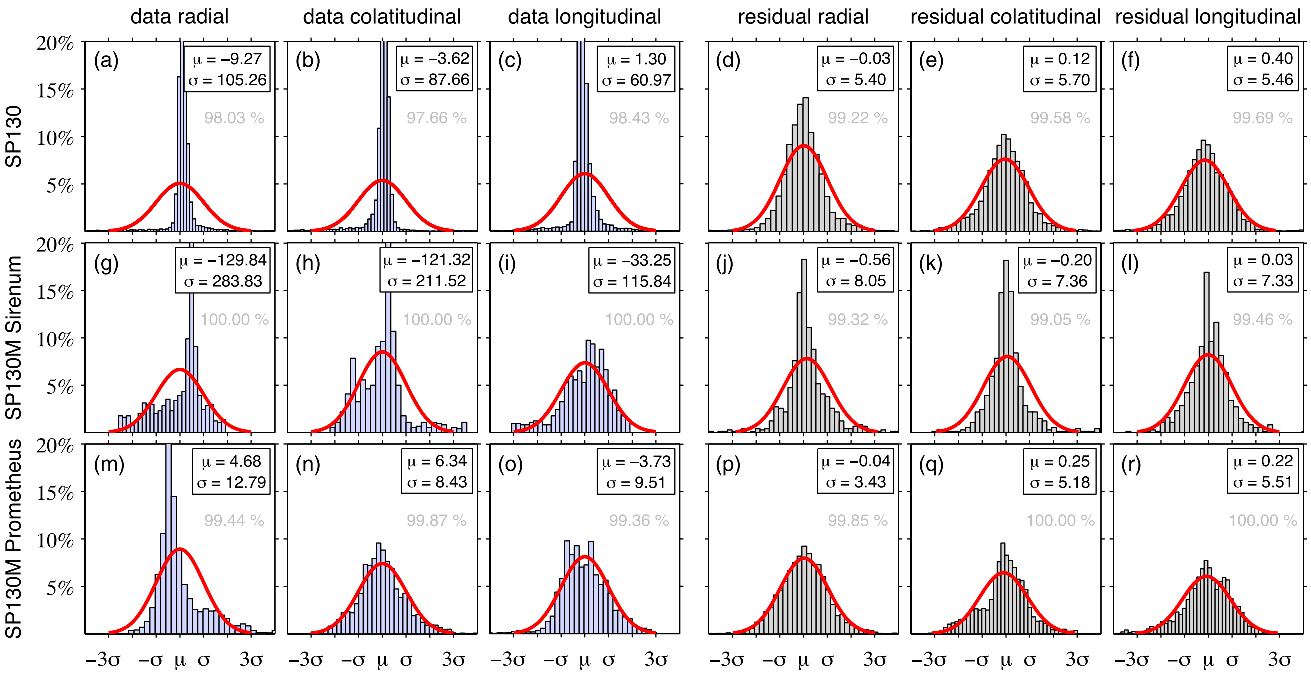

Figure A1. Distribution of data (Figures A1a–A1c, A1g–A1i, A1m–A1o) and residuals (Figures A1d–A1f, A1j–A1l, A1p–A1r), for the models SP130 (Figures A1a–A1f) and the two subregions of SP130M, Southern Terra Sirenum (Figures A1g–A1l) and Prometheus Planum (Figures A1m–A1r). Histograms are overlaid by the best fit normal distribution. All panels are centered on the means (μ), and their horizontal axes cover 4 standard deviations (σ) away from the means. The vertical axes are in percentage of the number of data points for each subregion, truncated to 20%, and the total percentage of data that falls in the range $\mu \pm 4\sigma$ is listed in gray. Boxed legends are in nT.

the colatitudinal and longitudinal components, almost normally distributed. Within this region, the residual distribution of the colatitudinal component (Figure A1q) is slightly asymmetric. The radial (Figure A1p) and longitudinal components (Figure A1r) closely follow a normal distribution.

Acknowledgments

We thank Nils Olsen for providing his Martian external field model [*Olsen et al.*, 2010], Achim Morschhauser for his global crustal magnetic field model [*Morschhauser et al.*, 2014] and for his comments that improved the paper, and Francis Nimmo and Edwin Kite for discussions. We also thank NASA for making MGS and other satellite and rover data publicly available on the Planetary Data System http://pds.nasa.gov, and the reviewers for their helpful and insightful comments. All maps in this article were made using the Generic Mapping Tools (GMT) [*Wessel et al.*, 2013]. This work was supported by NASA grant 13-MDAP13-0008. At the time of submission of this article, we are in the progress of preparing the software we developed for this research for public access in the same manner as we published our past software [*Harig et al.*, 2015]. For software and models that are not yet publicly available, please contact the corresponding author of this article.

References

Acuña, M. H., et al. (1998), Magnetic field and plasma observations at Mars: Initial results of the Mars Global Surveyor mission, *Science*, *279*(5357), 1676–1680, doi:10.1126/science.279.5357.1676.

Acuña, M. H., et al. (1999), Global distribution of crustal magnetization discovered by the Mars Global Surveyor MAG/ER experiment, *Science*, *284*(5415), 790–793, doi:10.1126/science.284.5415.790.

Acuña, M. H., et al. (2001), Magnetic field of Mars: Summary of results from the aerobraking and mapping orbits, *J. Geophys. Res.*, *106*(E10), 23,403–23,417, doi:10.1029/2000JE001404.

Allaire, G., and S. M. Kaber (2008), *Numerical Linear Algebra*, Springer.

Amit, H., U. R. Christensen, and B. Langlais (2011), The influence of degree-1 mantle heterogeneity on the past dynamo of Mars, *Phys. Earth Planet. Inter.*, *189*, 63–79, doi:10.1016/j.pepi.2011.07.008.

Arkani-Hamed, J. (2001a), A 50-degree spherical harmonic model of the magnetic field of Mars, *J. Geophys. Res.*, *106*(E10), 23,197–23,208, doi:10.1029/2000JE001365.

Arkani-Hamed, J. (2001b), Paleomagnetic pole positions and pole reversals of Mars, *Geophys. Res. Lett.*, *28*(17), 3409–3412, doi:10.1029/2001GL012928.

Arkani-Hamed, J. (2002), An improved 50-degree spherical harmonic model of the magnetic field of Mars derived from both high-altitude and low-altitude data, *J. Geophys. Res.*, *107*(E10), 13–1Ű-13-8, doi:10.1029/2001JE001835.

Arkani-Hamed, J. (2004), A coherent model of the crustal magnetic field of Mars, *J. Geophys. Res.*, *109*, E09005, doi:10.1029/2004JE002265.

Arkani-Hamed, J., and D. Boutin (2004), Paleomagnetic poles of Mars: Revisited, *J. Geophys. Res.*, *109*, E03011, doi:10.1029/2003JE002229.

Arkani-Hamed, J., and D. Boutin (2012), Is the primordial crust of Mars magnetized?, *Icarus*, *221*, 192–207, doi:10.1016/j.icarus.2012.07.030.

Backus, G. E., R. L. Parker, and C. G. Constable (1996), *Foundations of Geomagnetism*, Cambridge Univ. Press, Cambridge, U. K.

Beggan, C. D., J. Saarimäki, K. A. Whaler, and F. J. Simons (2013), Spectral and spatial decomposition of lithospheric magnetic field models using spherical Slepian functions, *Geophys. J. Int.*, *193*(1), 136–148, doi:10.1093/gji/ggs122.

Blakely, R. J. (1995), *Potential Theory in Gravity and Magnetic Applications*, Cambridge Univ. Press, New York.

Boutin, D., and J. Arkani-Hamed (2006), Pole wandering of Mars: Evidence from paleomagnetic poles, *Icarus*, *181*, 12–25, doi:10.1016/j.icarus.2005.10.025.

Brain, D. A., F. Bagenal, M. H. Acuña, and J. E. P. Connerney (2003), Martian magnetic morphology: Contributions from the solar wind and crust, *J. Geophys. Res.*, *108*(A12), 1424, doi:10.1029/2002JA009482.

Cain, J. C., B. B. Ferguson, and D. Mozzoni (2003), An n=90 internal potential function of the Martian crustal magnetic field, *J. Geophys. Res.*, *108*(E2), 5008, doi:10.1029/2000JE001487.

Chiao, L.-Y., J.-R. Lin, and Y.-C. Gung (2006), Crustal magnetization equivalent source model of Mars constructed from a hierarchical multiresolution inversion of the Mars Global Surveyor data, *J. Geophys. Res.*, *111*, E12010, doi:10.1029/2006JE002725.

Citron, R. I., and S. Zhong (2012), Constraints on the formation of the Martian crustal dichotomy from remnant crustal magnetism, *Phys. Earth Planet. Inter.*, *212*, 55–63, doi:10.1016/j.pepi.2012.09.008.

Connerney, J. E. P., et al. (1999), Magnetic lineations in the ancient crust of Mars, *Science*, *284*(5415), 794–798.

Connerney, J. E. P., M. H. Acuña, P. J. Wasilewski, G. Kletetschka, N. F. Ness, H. Rème, R. P. Lin, and D. L. Mitchell (2001), The global magnetic field of Mars and implications for crustal evolution, *Geophys. Res. Lett.*, *28*(21), 4051–4048, doi:10.1029/2001GL013619.

Connerney, J. E. P., M. H. Acuña, N. F. Ness, G. Kletetschka, D. L. Mitchell, R. P. Lin, and H. Rème (2005), Tectonic implications of Mars crustal magnetism, *Proc Natl. Acad. Sci.*, *102*(42), 14,970–14,975, doi:10.1073/pnas.0507469102.

Crider, D. H. (2004), The influence of crustal magnetism on the solar wind interaction with Mars: Recent observations, *Adv. Space Res.*, *33*, 152–160, doi:10.1016/j.asr.2003.04.013.

Dahlen, F. A., and F. J. Simons (2008), Spectral estimation on a sphere in geophysics and cosmology, *Geophys. J. Int.*, *174*, 774–807, doi:10.1111/j.1365-246X.2008.03854.x.

Dahlen, F. A., and J. Tromp (1998), *Theoretical Global Seismology*, Princeton Univ. Press., Princeton, N. J.

Di Achille, G., and B. M. Hynek (2010), Ancient ocean on Mars supported by global distribution of deltas and valleys, *Nature Geosci.*, *3*, 459–463, doi:10.1038/NGEO891.

Dietrich, W., and J. Wicht (2013), A hemispherical dynamo model: Implications for the Martian crustal magnetization, *Phys. Earth Planet. Inter.*, *217*, 10–21, doi:10.1016/j.pepi.2013.01.001.

Dunlop, D. J., and J. Arkani-Hamed (2005), Magnetic minerals in the Martian crust, *J. Geophys. Res.*, *110*, E12S04, doi:10.1029/2005JE002,404.

Fairén, A. G., J. Ruiz, and F. Anguita (2002), An origin for the linear magnetic anomalies on Mars through accretion of terranes: Implications for dynamo timing, *Icarus*, *160*, 220–223, doi:10.1006/icar.2002.6942.

Farquharson, C. G., and D. W. Oldenburg (1998), Non-linear inversion using general measures of data misfit and model structure, *Geophys. J. Int.*, *134*, 213–227, doi:10.1046/j.1365-246x.1998.00555.x.

Fastook, J. L., J. W. Head, D. R. Marchant, F. Forget, and J.-B. Madeleine (2012), Early Mars climate near the Noachian–Hesperian boundary: Independent evidence for cold conditions from basal melting of the south polar ice sheet (Dorsa Argentea Formation) and implications for valley network formation, *Icarus*, *219*, 25–40, doi:10.1016/j.icarus.2012.02.013.

Frawley, J. J., and P. T. Taylor (2004), Paleo-pole positions from Martian magnetic anomaly data, *Icarus*, *172*, 316–327, doi:10.1016/j.icarus.2004.07.025.

Gerhards, C. (2012), Locally supported wavelets for the separation of spherical vector fields with respect to their sources, *Int. J. Wavelets Multiresolut. Inf. Process.*, *10*(4), 1250,034, doi:10.1142/S0219691312500348.

Ghatan, G. J., J. W. Head, and S. Pratt (2003), Cavi Angusti, Mars: Characterization and assessment of possible formation mechanisms, *J. Geophys. Res.*, *108*(E5), 5045, doi:10.1029/2002JE001972.

Gilbert, F. (1971), Ranking and winnowing gross Earth data for inversion and resolution, *Geophys. J. Int.*, *23*(1), 125–128, doi:10.1111/j.1365-246X.1971.tb01807.x.

Harig, C., K. W. Lewis, A. Plattner, and F. J. Simons (2015), A suite of software analyzes data on the sphere, *Eos Trans. AGU*, *96*(6), 18–22, doi:10.1029/2015EO025851.

Harrison, C. G. A. (2000), Questions about magnetic lineations in the ancient crust of Mars, *Science*, *547a*, doi:10.1126/science.287.5453.547a.

Head, J. W., and S. Pratt (2001), Extensive Hesperian-aged south polar ice sheet on Mars: Evidence for massive melting and retreat, and lateral flow and ponding of meltwater, *J. Geophys. Res.*, *106*(E6), 12,275–12,299, doi:10.1029/2000JE001359.

Holschneider, M., A. Chambodut, and M. Mandea (2003), From global to regional analysis of the magnetic field on the sphere using wavelet frames, *Phys. Earth Planet. Inter.*, *135*, 107–124.

Hood, L. L., and A. Zakharian (2001), Mapping and modeling of magnetic anomalies in the northern polar region of Mars, *J. Geophys. Res.*, *106*(E7), 14,601–14,619, doi:10.1029/2000JE001304.

Hood, L. L., C. N. Young, N. C. Richmond, and K. P. Harrison (2005), Modeling of major Martian magnetic anomalies: Further evidence for polar reorientations during the Noachian, *Icarus*, *177*(1), 144–173, doi:10.1016/j.icarus.2005.02.008.

Hood, L. L., N. C. Richmond, K. P. Harrison, and R. J. Lillis (2007), East–west trending magnetic anomalies in the southern hemisphere of Mars: Modeling analysis and interpretation, *Icarus*, *191*(1), 113–131, doi:10.1016/j.icarus.2007.04.025.

Hood, L. L., K. P. Harrison, B. Langlais, R. J. Lillis, F. Poulet, and D. A. Williams (2010), Magnetic anomalies near Apollinaris Patera and the Medusae Fossae Formation in Lucus Planum, Mars, *Icarus*, *208*(1), 118–131, doi:10.1016/j.icarus.2010.01.009.

Hynek, B. M., S. J. Robbins, O. Šrámek, and S. Zhong (2011), Geological evidence for a migrating Tharsis plume on early Mars, *Earth Planet. Sci. Lett.*, *310*, 327–333, doi:10.1016/j.epsl.2011.08.020.

Jahn, K., and N. Bokor (2012), Vector Slepian basis functions with optimal energy concentration in high numerical aperture focusing, *Optics Comm.*, *285*, 2028–2038, doi:10.1016/j.optcom.2011.11.107.

Johnson, C. L., and R. J. Phillips (2005), Evolution of the Tharsis region of Mars: Insights from magnetic field observations, *Earth Planet. Sci. Lett.*, *230*, 241–254, doi:10.1016/j.epsl.2004.10.038.

Kaula, W. M. (1967), Theory of statistical analysis of data distributed over a sphere, *Rev. Geophys.*, *5*(1), 83–107, doi:10.1029/RG005i001p00083.

Langlais, B., and M. Purucker (2007), A polar magnetic paleopole associated with Apollinaris Patera, Mars, *Planet. Space Sci.*, *55*, 270–279, doi:10.1016/j.pss.2006.03.008.

Langlais, B., and Y. Quesnel (2008), New perspectives on Mars' crustal magnetic field, *C. R. Geosci.*, *340*, 791–800, doi:10.1016/j.crte.2008.08.006.

Langlais, B., M. E. Purucker, and M. Mandea (2004), Crustal magnetic field of Mars, *J. Geophys. Res.*, *E02,008*(E2), doi:10.1029/2003JE002048.

Lesur, V. (2006), Introducing localized constraints in global geomagnetic field modelling, *Earth Planets Space*, *58*(4), 477–483.

Lesur, V., and S. Maus (2006), A global lithospheric magnetic field model with reduced noise level in the Polar Regions, *Geophys. Res. Lett.*, *33*, L13304, doi:10.1029/2006GL025826.

Lewis, K. W., and F. J. Simons (2012), Local spectral variability and the origin of the Martian crustal magnetic field, *Geophys. Res. Lett.*, *39*, L18201, doi:10.1029/2012GL052708.

Lillis, R. J., D. L. Mitchell, R. P. Lin, J. E. P. Connerney, and M. H. Acuña (2004), Mapping crustal magnetic fields at Mars using electron reflectometry, *Geophys. Res. Lett.*, *31*, L15702, doi:10.1029/2004GL020189.

Lillis, R. J., H. V. Frey, M. Manga, D. L. Mitchell, R. P. Lin, M. H. Acuña, and S. W. Bougher (2008a), An improved crustal magnetic field map of Mars from electron reflectometry: Highland volcano magmatic history and the end of the Martian dynamo, *Icarus*, *194*(2), 575–596, doi:10.1016/j.icarus.2007.09.032.

Lillis, R. J., S. W. Bougher, D. L. Mitchell, D. A. Brain, R. P. Lin, and M. H. Acuña (2008b), Continuous monitoring of nightside upper thermospheric mass densities in the Martian southern hemisphere over 4 Martian years using electron reflectometry, *Icarus*, *194*, 562–574, doi:10.1016/j.icarus.2007.09.031.

Lillis, R. J., J. Dufek, J. E. Bleacher, and M. Manga (2009), Demagnetization of crust by magmatic intrusion near the Arsia Mons volcano: Magnetic and thermal implications for the development of the Tharsis province, Mars, *J. Volcanol. Geoth. Res.*, *185*, 123–138, doi:10.1016/j.jvolgeores.2008.12.007.

Lillis, R. J., M. E. Purucker, J. S. Halekas, K. L. Louzada, S. T. Stewart-Mukhopadhyay, M. Manga, and H. V. Frey (2010), Study of impact demagnetization at Mars using Monte Carlo modeling and multiple altitude data, *J. Geophys. Res.*, *115*, E07007, doi:10.1029/2009JE003556.

Lillis, R. J., S. Robbins, M. Manga, J. S. Halekas, and H. V. Frey (2013), Time history of the Martian dynamo from crater magnetic field analysis, *J. Geophys. Res. Planets*, *118*, 1488–1511, doi:10.1002/jgre.20105.

Mayer, C., and T. Maier (2006), Separating inner and outer Earth's magnetic field from CHAMP satellite measurements by means of vector scaling functions and wavelets, *Geophys. J. Int.*, *167*, 1188–1203, doi:10.1111/j.1365-246X.2006.03199.x.

Milbury, C., and G. Schubert (2010), Search for the global signature of the Martian dynamo, *J. Geophys. Res.*, *115*(E10), E10010, doi:10.1029/2010JE003617.

Milbury, C., G. Schubert, C. A. Raymond, S. E. Smrekar, and B. Langlais (2012), The history of Mars' dynamo as revealed by modeling magnetic anomalies near Tyrrhenus Mons and Syrtis Major, *J. Geophys. Res.*, *117*, E10007, doi:10.1029/2012JE004099.

Milkovich, S. M., and J. J. Plaut (2008), Martian south polar layered deposit stratigraphy and implications for accumulation history, *J. Geophys. Res.*, *113*, E06007, doi:10.1029/2007JE002987.

Milkovich, S. M., J. W. Head, and S. Pratt (2002), Meltback of Hesperian-aged ice-rich deposits near the south pole of Mars: Evidence for drainage channels and lakes, *J. Geophys. Res.*, *107*(E6), 10–1–10–13, doi:10.1029/2001JE001802.

Mitchell, D. L., R. J. Lillis, R. P. Lin, J. E. P. Connerney, and M. H. Acuña (2007), A global map of Mars' crustal magnetic field based on electron reflectometry, *J. Geophys. Res.*, *112*, E01002, doi:10.1029/2005JE002564.

Morschhauser, A., V. Lesur, and M. Grott (2014), A spherical harmonic model of the lithospheric magnetic field of Mars, *J. Geophys. Res. Planets*, *119*(6), 1162–1188, doi:10.1002/2013JE004555.

Nimmo, F. (2000), Dike intrusion as a possible cause of linear Martian magnetic anomalies, *Geology*, *28*(5), 391–394.

Nimmo, F., and M. S. Gilmore (2001), Constraints on the depth of magnetized crust on Mars from impact craters, *J. Geophys. Res.*, *106*(E6), 12,315–12,323, doi:10.1029/2000JE001325.

Nimmo, F., and D. J. Stevenson (2001), Estimates of Martian crustal thickness from viscous relaxation of topography, *J. Geophys. Res.*, *106*(E3), 5085–5098, doi:10.1029/2000JE001331.

Nimmo, F., and K. Tanaka (2005), Early crustal evolution of Mars, *Annu. Rev. Earth. Planet. Sc.*, *33*, 133–161, doi:10.1146/annurev.earth.33.092203.122637.

Olsen, N., K.-H. Glassmeier, and X. Jia (2010), Separation of the magnetic field into external and internal parts, *Space Sci. Rev.*, *152*, 135–157, doi:10.1007/s11214-009-9563-0.

Perron, J. T., J. X. Mitrovica, M. Manga, I. Matsuyama, and M. A. Richards (2007), Evidence for an ancient Martian ocean in the topography of deformed shorelines, *Nature*, *447*, 840–843, doi:10.1038/nature05873.

Plattner, A., and F. J. Simons (2014a), Potential-field estimation using scalar and vector Slepian functions at satellite altitude, in *Handbook of Geomathematics*, edited by W. Freeden, M. Z. Nashed, and T. Sonar, Springer, Heidelberg, Germany, doi:10.1007/978-3-642-27793-1_64-2.

Plattner, A., and F. J. Simons (2014b), Spatiospectral concentration of vector fields on a sphere, *Appl. Comput. Harmon. Anal.*, *36*, 1–22, doi:10.1016/j.acha.2012.12.001.

Plattner, A., F. J. Simons, and L. Wei (2012), Analysis of real vector fields on the sphere using Slepian functions, in *2012 IEEE Statistical Signal Processing Workshop (SSP'12) IEEE*, Ann Arbor, Mich.

Purucker, M., D. Ravat, H. Frey, C. Voorhies, T. Sabaka, and M. Acuña (2000), An altitude-normalized magnetic map of Mars and its interpretation, *Geophys. Res. Lett.*, *27*(16), 2449–2452, doi:10.1029/2000GL000072.

Quesnel, Y., B. Langlais, and C. Sotin (2007), Local inversion of magnetic anomalies: Implication for Mars' crustal evolution, *Planet. Space Sci.*, *55*, 258–269, doi:10.1016/j.pss.2006.02.004.

Ravat, D. (2011), Interpretation of Mars southern highlands high amplitude magnetic field with total gradient and fractal source modeling: New insights into the magnetic mystery of Mars, *Icarus*, *214*, 400–412, doi:10.1016/j.icarus.2011.05.004.

Schachtschneider, R., M. Holschneider, and M. Mandea (2010), Error distribution in regional inversion of potential field data, *Geophys. J. Int.*, *181*, 1428–1440, doi:10.1111/j.1365-246X.2010.04598.x.

Schachtschneider, R., M. Holschneider, and M. Mandea (2012), Error distribution in regional modelling of the geomagnetic field, *Geophys. J. Int.*, *191*, 1015–1024, doi:10.1111/j.1365-246X.2012.05675.x.

Schott, J.-J., and E. Thébault (2011), Modelling the Earth's magnetic field from global to regional scales, in *Geomagnetic Observations and Models*, edited by J.-J. Schott and E. Thébault, IAGA Special Sopron Book Ser., vol. 5, 229–264, Springer.

Simons, F. J., and F. A. Dahlen (2006), Spherical Slepian functions and the polar gap in geodesy, *Geophys. J. Int.*, *166*, 1039–1061, doi:10.1111/j.1365-246X.2006.03065.x.

Simons, F. J., F. A. Dahlen, and M. A. Wieczorek (2006), Spatiospectral concentration on a sphere, *SIAM Rev.*, *48*(3), 504–536, doi:10.1137/S0036144504445765.

Slepian, D. (1983), Some comments on Fourier analysis, uncertainty and modeling, *SIAM Rev.*, *25*(3), 379–393.

Smith, D. E., et al. (1999), The global topography of Mars and implications for surface evolution, *Science*, *284*(5419), 1495–1503.

Sprenke, K. F., and L. L. Baker (2000), Magnetization, paleomagnetic poles, and polar wander on Mars, *Icarus*, *147*(1), 26–34, doi:10.1006/icar.2000.6439.

Stanley, S., L. Elkins-Tanton, M. T. Zuber, and E. M. Parmentier (2008), Mars paleomagnetic field as the result of a single-hemisphere dynamo, *Science*, *321*, 1822–1825.

Stevenson, D. J. (2001), Mars' core and magnetism, *Nature*, *412*, 214–219, doi:10.1038/35084155.

Tanaka, K. L., J. A. Skinner, J. M. Dohm, R. P. Irwin, E. J. Kolb, C. M. Fortezzo, T. Platz, G. G. Michael, and T. M. Hare (2014), *Geologic Map of Mars*, 43, U. S. Geological Survey Scientific Investigations Map 3292, scale 1:20,000,000, pamphlet.

Thébault, E (2008), A proposal for regional modelling at the Earth's surface, R-SCHA2D, *Geophys. J. Int.*, *174*, 118–134, doi:10.1111/j.1365-246X.2008.03823.x.

Thébault, E., J. J. Schott, and M. Mandea (2006), Revised spherical cap harmonic analysis (R-SCHA): Validation and properties, *J. Geophys. Res.*, *111*(B1), B01102, doi:10.1029/2005JB003836.

Voorhies, C. V. (2008), Thickness of the magnetic crust of Mars, *J. Geophys. Res.*, *113*, E04004, doi:10.1029/2007JE002928.

Voorhies, C. V., T. J. Sabaka, and M. Purucker (2002), On magnetic spectra of Earth and Mars, *J. Geophys. Res.*, *107*(E6), 5034, doi:10.1029/2001JE001534.

Weiss, B. P., H. Vali, F. J. Baudenbacher, J. L. Kirschvink, S. T. Stewart, and D. L. Shuster (2002), Records of an ancient Martian magnetic field in ALH84001, *Earth Planet. Sci. Lett.*, *201*, 449–463.

Wessel, P., W. H. F. Smith, R. Scharroo, J. Luis, and F. Wobbe (2013), Generic Mapping Tools: Improved version released, *Eos Trans. AGU*, *94*(45), 409–410, doi:10.1002/2013EO450001.

Whaler, K. A., and D. Gubbins (1981), Spherical harmonic analysis of the geomagnetic field: An example of a linear inverse problem, *Geophys. J. Int.*, *65*(3), 645–693, doi:10.1111/j.1365-246X.1981.tb04877.x.

Whaler, K. A., and M. E. Purucker (2005), A spatially continuous magnetization model for Mars, *J. Geophys. Res.*, *110*, E09,001, doi:10.1029/2004JE002393.

Wieczorek, M. A., and F. J. Simons (2005), Localized spectral analysis on the sphere, *Geophys. J. Int.*, *162*(3), 655–675, doi:10.1111/j.1365-246X.2005.02687.x.

Wieczorek, M. A., and F. J. Simons (2007), Minimum-variance spectral analysis on the sphere, *J. Fourier Anal. Appl.*, *13*(6), 665–692, doi:10.1007/s00,041-006-6904-1.

Williams, J.-P., and F. Nimmo (2004), Thermal evolution of the Martian core: Implications for an early dynamo, *Geology*, *32*(2), 97–100, doi:10.1130/G19975.1.